

TRUNCATED NONSMOOTH NEWTON MULTIGRID FOR PHASE-FIELD BRITTLE-FRACTURE PROBLEMS

CARSTEN GRÄSER, DANIEL KIENLE, AND OLIVER SANDER

ABSTRACT. We propose the Truncated Nonsmooth Newton Multigrid Method (TNNMG) as a solver for the spatial problems of the small-strain brittle-fracture phase-field equations. TNNMG is a nonsmooth multigrid method that can solve biconvex, block-separably nonsmooth minimization problems in roughly the time of solving one linear system of equations. It exploits the variational structure inherent in the problem, and handles the pointwise irreversibility constraint on the damage variable directly, without regularization or the introduction of a local history field. Memory consumption is significantly lower compared to approaches based on direct solvers. In the paper we introduce the method and show how it can be applied to several established models of phase-field brittle fracture. We then prove convergence of the solver to a solution of the nonsmooth Euler–Lagrange equations of the spatial problem for any load and initial iterate. Numerical comparisons to an operator-splitting algorithm show a speed increase of more than one order of magnitude, without loss of robustness.

Keywords: phase field, brittle fracture, spectral strain decomposition, nonsmooth multigrid, global convergence

1. INTRODUCTION

The equations of phase-field models of brittle fracture present a number of challenges to the designers of numerical solution algorithms [1]. Even in the small-strain case the equations are nonlinear, due to the multiplicative coupling of the mechanical stresses to the degradation function. At the same time the non-healing condition introduces an inequality constraint. Finally, eigenvalue-based splittings of the energy density as in [24] make the equations nondifferentiable.

In this paper we focus on the spatial problems of small-strain brittle-fracture phase-field models obtained by a suitable time discretization. The standard approach to solving these spatial problems is based on operator splitting. Algorithms based on this approach, also known as staggered schemes, alternate between solving a displacement problem with fixed damage and a damage problem with fixed displacement. Both subproblems are elliptic and well-understood, and such methods are therefore straightforward to implement. The method can be interpreted as a nonlinear Gauß–Seidel method [9], which provides a natural framework for convergence proofs. Applications of the operator splitting scheme and its extensions appear, e.g., in [5, 7]. With particular semi-implicit time discretizations it is also possible to solve the spatial problems by solving only one damage problem and one

The authors gratefully acknowledge the financial support by the German Federal Ministry of Education and Research through the ParaPhase project within the framework “IKT 2020 – Forschung für Innovationen” (project numbers 01-H15005C, 01-15005D, 01-15005E).

displacement problem [23]. This is very fast, but works only if the load steps are small enough.

In contrast, other works propose monolithic solution schemes based on Newton’s method [9, 10, 36, 37]. For the unmodified Newton method only local convergence can be shown, and failure to converge for large load steps is readily observed in practice [39]. Therefore, various authors have proposed extensions or modifications of the Newton idea to stabilize the method. In [10] a line search strategy is applied to enlarge the domain of convergence of Newton’s method. Wu et al. [39] propose to use the BFGS quasi-Newton algorithm, claiming that it is more stable than Newton’s method and more efficient than operator splitting. Heister et al. [17] proposed a modified Newton scheme which was later improved by Wick [37] with an adaptive transition from Newton’s method to the modified Newton scheme. Finally, the authors of [22, 31] suggest an arc-length method based on the fracture surface, and an adaptive time stepping scheme to enhance the robustness. In summary, while monolithic Newton-type methods are reported to be faster than operator-splitting algorithms, the latter ones are more robust [1, 39].

Various approaches are used in the literature to deal with the damage irreversibility. A natural approach is to regularize the constraint, as investigated in [24, 35]. This leads to an additional parameter, and to ill-conditioned tangent matrices [11]. A second approach considers the thermodynamic driving force of the fracture phase-field as a global unknown yielding a three-field formulation which results in a saddle-point principle [24]. A third formulation considers the Karush–Kuhn–Tucker conditions and shifts the thermodynamic driving force of the fracture phase-field into a local history field representing the maximum over time of the elastic energy [23]. This approach, frequently known as the \mathcal{H} -field technique, therefore trades the inequality constraint for the nondifferentiable maximum function. Unfortunately, this approach spoils the variational structure of the spatial problems.

Augmented Lagrangian solvers as in [35] introduce extra variables. Closest in spirit to the present manuscript is the use of bound-constrained optimization solvers, used, e.g., in [2, 9, 38]. None of these approaches are fully satisfactory.

The effect of the nondifferentiable terms caused by anisotropic splits of the mechanical energy density as in [2, 24, 32] is rarely discussed in the literature. Hybrid formulations like the one proposed in [1] try to overcome the additional computational difficulties of these splits by further changes to the model, again at the cost of sacrificing the variational structure.

All these approaches are slow in the sense that they have to solve global partial differential equations at each Newton or operator-splitting iteration. When the methods use direct sparse solvers for the linear tangent problems, memory consumption can become problematic, too. At the same time, the problem of small-strain phase-field brittle fracture has a lot of elegant variational structure; in particular, it fits directly into the rate-independent framework of Mielke and Roubíček [25]. As a consequence, implicit time discretization leads to a sequence of coercive minimization problems for the displacement and damage fields together. These problems are not convex, but they are biconvex, i.e., convex (even strongly convex) in each variable separately. Pointwise inequality restrictions $\dot{d} \geq 0$ to handle the irreversibility of the fracture process as proposed in [24] reduce the smoothness of the objective functional, but do not influence its convexity or coercivity properties. The same

holds for anisotropic energy splits based on linear quantities or the eigenvalues of the mechanical strain.

Recent years have shown that nonsmooth multigrid are able to solve nonsmooth problems from mechanics efficiently without the need for solving global linear systems of equations [13, 15, 16, 18, 19, 30]. This makes them vastly more efficient than operator-splitting or Newton-based methods. As there are no sparse matrix factorizations, memory consumption remains low. In addition, these multigrid methods can be shown to converge globally, i.e., from any initial iterate, and for any load step. The proof exploits the above-mentioned variational structure, together with certain separability properties. As one such method, the Truncated Nonsmooth Newton Multigrid method (TNNMG) can treat the pointwise constraints of the increment problems directly, i.e., without artificial regularization or tricks like the \mathcal{H} -field technique [23]. The idea is that TNNMG only needs to handle these constraints in a series of low-dimensional subproblems, each of which is easy to solve by itself. As a consequence, solving the problems with constraints is not appreciably slower than solving the corresponding unconstrained problem.

In this paper we show how the TNNMG method can be used to solve small-strain brittle-fracture problems. This involves in particular verifying that the increment functionals have the required convexity and smoothness properties. We do this for a range of different degradation functions and local crack surface densities (including the standard Ambrosio–Tortorelli functionals of type 1 and 2). We cover elastic energies with various types of anisotropic splits, including the split based on strain eigenvalues of Miehe et al. [24]. For the proofs we use results from the convex analysis of spectral functions [3, 27]. In contrast to multilevel trust region methods [18] the TNNMG method proposed here relies on nonsmooth Newton techniques leading to linear subproblems and thus gives more flexibility in the selection of coarse grid solvers.

The paper is organized as follows: Chapter 2 discusses a framework of small-strain phase-field models for brittle fracture, and shows the range of applicability of the TNNMG solver. Chapter 3 introduces the natural fully implicit time discretization, and proves existence of solutions for the spatial problems. In both chapters we pay particular attention to the mathematical properties of the energy functionals. In Chapter 4, finally, we introduce the TNNMG method. We explain its construction, discuss various algorithmic options, and prove that it converges globally to stationary points of the increment energy functional. The numerical efficiency is then demonstrated in Chapter 5. Our reference for comparison is the operator-splitting iteration of the \mathcal{H} -field formulation of Miehe et al. [23], which we briefly revisit in Section 5.1. We compare the solvers for two- and three-dimensional example problems with different forms of the local crack surface density, and with and without spectral splits. We observe a considerable performance increase, without loss of robustness.

2. PHASE-FIELD MODELS OF BRITTLE FRACTURE

This chapter presents a range of phase-field models for brittle fracture, and discusses its smoothness and convexity properties.

Consider a deformable m -dimensional object represented by a domain $\Omega \in \mathbb{R}^m$. The deformation of such an object is characterized by a displacement field \mathbf{u} :

$\Omega \rightarrow \mathbb{R}^m$. The object is supposed to exhibit small-strain deformations and elastic material behavior only, and we therefore introduce the linearized strain tensor $\boldsymbol{\varepsilon}(\mathbf{u}) := \frac{1}{2}(\nabla \mathbf{u} + \nabla \mathbf{u}^T)$. Following [24], we model the fracturing by a scalar damage field $d : \Omega \rightarrow [0, 1]$, where $d = 0$ signifies intact material, and $d = 1$ a fully broken one. Dirichlet boundary conditions can be posed both for the displacement and for the damage field. For this we select two not necessarily equal subsets $\Gamma_{D,\mathbf{u}}, \Gamma_{D,d} \subset \partial\Omega$ of the domain boundary, and require

$$\mathbf{u} = \mathbf{u}_0 \quad \text{on } \Gamma_{D,\mathbf{u}}, \quad d = d_0 \quad \text{on } \Gamma_{D,d},$$

where \mathbf{u}_0 and d_0 are two given functions.

Displacement and damage field evolve together, governed by a system of coupled nonsmooth partial differential equations. Disregarding inertia effects, we obtain a rate-independent system in the sense of Mielke and Roubíček [25]. Such a system can be written using the Biot equation

$$(1) \quad \partial_{\dot{d}} \mathcal{R}(d, \dot{d}) + D_{(\mathbf{u},d)} \mathcal{E}(t, \mathbf{u}, d) \ni 0,$$

where $D_{(\mathbf{u},d)} \mathcal{E}(t, \mathbf{u}, d)$ means the Gâteaux derivative with respect to the second and third arguments of \mathcal{E} , and $\partial_v \mathcal{R}(d, v)$ is the convex subdifferential with respect to the second argument of the dissipation potential \mathcal{R} .

In this equation, \mathcal{E} is a potential energy, which we assume to be of the form

$$(2) \quad \mathcal{E}(t, \mathbf{u}, d) = \int_{\Omega} \psi(\boldsymbol{\varepsilon}(\mathbf{u}), d) dV + \int_{\Omega} g_c \gamma(d, \nabla d) dV + P_{\text{ext}}(t, \mathbf{u}) + \int_{\Omega} I_{[0,1]}(d) dV.$$

The term ψ is a degraded elastic energy density, and will be discussed in detail in Section 2.1. The term γ models the local crack surface density, and will be discussed in Section 2.2. The number g_c is Griffith's critical energy release rate, a material parameter. P_{ext} represents time-dependent volume and surface forces, which drive the evolution. We assume that P_{ext} is linear and $H^1(\Omega)$ -continuous in \mathbf{u} , and differentiable in t with bounded time derivative.

The last term of (2) implements the restriction that the damage field can only assume values between 0 and 1. For a set $\mathcal{K} \subset \mathbb{R}$ we define the indicator functional

$$I_{\mathcal{K}} : \mathbb{R} \rightarrow \mathbb{R} \cup \{\infty\}, \quad I_{\mathcal{K}}(x) := \begin{cases} 0 & \text{if } x \in \mathcal{K}, \\ \infty & \text{otherwise.} \end{cases}$$

For a closed, convex, nonempty set \mathcal{K} , the functional $I_{\mathcal{K}}$ is convex, lower semi-continuous, and proper. Adding the constraint $d \in [0, 1]$ explicitly is not always necessary, as some fracture models lead to evolutions that satisfy the constraints implicitly. However, as pointwise bounds come with practically no cost when using the TNNMG solver, we do include them to extend our range of models.

To make the potential energy \mathcal{E} well defined, we will in general consider it on the first-order Sobolev space $H^1(\Omega, \mathbb{R}^m \times \mathbb{R})$. Incorporating the boundary conditions leads to the affine subspace

$$\mathbf{H}_{\mathbf{u}_0}^1 \times H_{d_0}^1 := \left\{ \mathbf{v} \in H^1(\Omega, \mathbb{R}^m) \mid \mathbf{v}|_{\Gamma_{D,\mathbf{u}}} = \mathbf{u}_0 \right\} \times \left\{ v \in H^1(\Omega) \mid v|_{\Gamma_{D,d}} = d_0 \right\}.$$

The second term of the Biot equation (1) is $\partial_{\dot{d}} \mathcal{R}(d, \dot{d})$, where \mathcal{R} is the dissipation potential

$$(3) \quad \mathcal{R}(d, \dot{d}) = \int_{\Omega} I_{[0,\infty)}(\dot{d}) dV.$$

It implements the pointwise non-healing condition \dot{d} as proposed by [24]. Note that $\mathcal{R}(d, \cdot) : H^1(\Omega) \rightarrow [0, \infty]$ is convex and lower semicontinuous, and $\mathcal{R}(d, 0) = 0$. The fact that \mathcal{R} is positively 1-homogeneous implies the rate-independence of the system.

Remark 2.1. In the engineering literature, the same problem is frequently formulated as

$$\partial_{(\dot{\mathbf{u}}, \dot{d})} \Pi(\dot{\mathbf{u}}, \dot{d}; \mathbf{u}, d) \ni 0,$$

with the rate potential

$$\begin{aligned} \Pi(\dot{\mathbf{u}}, \dot{d}; \mathbf{u}, d) &:= \frac{d}{dt} \mathcal{E}(t, \mathbf{u}, d) + \mathcal{R}(d, \dot{d}) \\ (4) \quad &= \frac{d}{dt} \int_{\Omega} \psi(\boldsymbol{\varepsilon}(\mathbf{u}), d) dV + \int_{\Omega} g_c \frac{d}{dt} \gamma(d, \nabla d) dV + P_{\text{ext}}(t, \dot{\mathbf{u}}) \\ &\quad + \int_{\Omega} I_{[0,1]}(d) dV + \int_{\Omega} I_{[0,\infty)}(\dot{d}) dV. \end{aligned}$$

This formulation is equivalent to the Biot equation (1) if the problem is sufficiently smooth.

We now in turn discuss the potential energy and the dissipation potential.

2.1. Degraded elastic energy density. We consider models that behave linearly elastic and isotropic if the material is in an undamaged state. That is, for the undamaged stored energy density we use the St. Venant–Kirchhoff material law, whose energy density is given by

$$\psi_0(\boldsymbol{\varepsilon}) = \frac{\lambda}{2} \text{tr}[\boldsymbol{\varepsilon}]^2 + \mu \text{tr}[\boldsymbol{\varepsilon}^2],$$

with Lamé parameters $\mu > 0$ and $\lambda > -\frac{2}{3}\mu$. With this choice of parameters the quadratic functional ψ_0 is strongly convex on \mathbb{S}^m .

The undamaged energy density is split as

$$\psi_0(\boldsymbol{\varepsilon}) = \psi_0^+(\boldsymbol{\varepsilon}) + \psi_0^-(\boldsymbol{\varepsilon})$$

into a part ψ_0^+ that produces damage and another part ψ_0^- that does not. The damage-producing part is then scaled by a so-called degradation function

$$g : [0, 1] \rightarrow [0, 1],$$

and the energy density $\psi : \mathbb{S}^m \times [0, 1] \rightarrow \mathbb{R}$ takes the form

$$(5) \quad \psi(\boldsymbol{\varepsilon}, d) = [g(d) + k] \psi_0^+(\boldsymbol{\varepsilon}) + \psi_0^-(\boldsymbol{\varepsilon}),$$

where $\mathbb{S}^m \subset \mathbb{R}^{m \times m}$ is the space of symmetric $m \times m$ matrices. The residual stiffness $k > 0$ guarantees a well-posed problem in case of fracture.

Various different degradation functions have appeared in the literature [20, 32]. While the details vary, there appears to be agreement on the following properties:

Assumption 2.1. *The degradation function $g : [0, 1] \rightarrow [0, 1]$ is differentiable, monotone decreasing, and fulfills $g(0) = 1$ and $g(1) = 0$.*

Note that several authors require $g'(1) = 0$ in order to ensure that the evolution does not lead to values of d larger than 1. We do not need this assumption here, because the pointwise constraint $d \leq 1$ is enforced explicitly by the energy term (2).

The following specific degradation functions all fulfill Assumption 2.1:

$$\begin{aligned} g_a(d) &= (1-d)^2 && \text{(from [6])} \\ g_b(d) &= (1-d)^2 \cdot (2d+1) && \text{(from [20])} \\ g_c(d) &= (1-d)^3 \cdot (3d+1) && \text{(from [20])} \\ g_d(d) &= \frac{\exp(bd) - (b(d-1)+1)\exp(b)}{(b-1)\exp(b)+1}, \quad b > 0 && \text{(from [32]).} \end{aligned}$$

Note that the functions g_a and g_d are strictly convex, but g_b and g_c are not even convex. For the rest of the paper we will restrict our considerations to convex twice continuously differentiable degradation functions g .

Various splittings of ψ_0 have been proposed in the literature. We cover four common strain-based splittings taking the form (5).¹ All those splitting have the property that $\psi_0 = \psi_0^+ + \psi_0^-$, and we will show that all have the following essential properties:

- (P₁) $\psi(\varepsilon, \cdot) \in C^2$ for all $\varepsilon \in \mathbb{S}^m$ and $\psi(\cdot, d) \in LC^1$ for all $d \in [0, 1]$, i.e., $\psi(\cdot, d)$ is differentiable with locally Lipschitz continuous derivative.
- (P₂) The gradient $\nabla\psi(\cdot, d)$ is semismooth for all $d \in [0, 1]$.
- (P₃) The gradient $\nabla\psi(\cdot, d)$ is globally Lipschitz continuous uniformly in d , i.e., there exists $L \geq 0$ independent of d such that for all matrices $A, B \in \mathbb{S}^m$ we have

$$|\nabla\psi(A, d) - \nabla\psi(B, d)| \leq L|A - B|_F.$$

- (P₄) $\psi(\cdot, d) : \mathbb{S}^m \rightarrow \mathbb{R}$ is strongly convex uniformly in d , i.e., there exists $\eta > 0$ independent of d such that for all matrices $A, B \in \mathbb{S}^m$ we have

$$\psi(tA + (1-t)B, d) \leq t\psi(A, d) + (1-t)\psi(B, d) - \frac{1}{2}\eta t(1-t)|A - B|_F^2.$$

- (P₅) $\psi(\cdot, d)$ is coercive uniformly in d in the sense that there exists $C > 0$ independent of d such that $\psi(\varepsilon, d) \geq C|\varepsilon|_F^2$.

We remind that the gradient $\nabla\psi(\cdot, d)$ is called semismooth if the limit

$$\lim_{\substack{G \in \partial(\nabla\psi(\cdot, d))(A+tV) \\ \tilde{V} \rightarrow V, t \searrow 0}} G\tilde{V}$$

exists for any point $A \in \mathbb{S}^m$ and any direction $V \in \mathbb{S}^m$. The set $\partial(\nabla\psi(\cdot, d))(A)$ denotes Clarke's generalized Jacobian of the locally Lipschitz continuous map $\nabla\psi(\cdot, d) : \mathbb{S}^m \rightarrow \mathbb{S}^m$ at $A \in \mathbb{S}^m$ (cf. [28]). Notice that the strong convexity (P₄) implies strong monotonicity of $\nabla\psi$, i.e.,

$$\langle \nabla\psi(A) - \nabla\psi(B), A - B \rangle \geq \eta|A - B|_F^2.$$

For the splittings considered in the following we will only prove (P₁) and (P₂) directly, and show that the simplified assumptions of the following lemma hold true. This then implies (P₃), (P₄), and (P₅).

Lemma 1. Let ψ_0^+ and ψ_0^- be convex, non-negative, and differentiable with Lipschitz continuous gradients $\nabla\psi_0^+$ and $\nabla\psi_0^-$. Then ψ satisfies (P₃), (P₄), and (P₅).

¹The stress-based splitting of Steinke and Kaliske [32] is left for future work.

Proof. Let L^+ and L^- be the Lipschitz constants of $\nabla\psi_0^+$ and $\nabla\psi_0^-$, respectively. Then $\nabla\psi(\cdot, d)$ is Lipschitz continuous with uniform Lipschitz constant $(1+k)L^+ + L^-$, because $g(d) + k \leq 1 + k$.

To show strong convexity, we first note that $\psi_0 = \psi_0^+ + \psi_0^-$ is strongly convex on \mathbb{S}^m with a modulus $\eta > 0$ independent of d . Now consider the function

$$\varepsilon \mapsto \psi(\varepsilon, d) - C\psi_0(\varepsilon) = (g(d) + k - C)\psi_0^+(\varepsilon) + (1 - C)\psi_0^-(\varepsilon)$$

for $0 < C = \min\{k, 1\} \leq g(d) + k$. Since this is a weighted sum of two convex functions ψ_0^+ and ψ_0^- with non-negative weights $g(d) + k - C \geq 0$ and $1 - C \geq 0$, it is itself convex. Thus, as a sum of this convex function and the strongly convex functions $C\psi_0$, the function $\psi(\cdot, d)$ is itself strongly convex and inherits the convexity modulus $C\eta$ of $C\psi_0$. Finally, we note that with the same C and η we have

$$\psi(\varepsilon, d) \geq C\psi_0(\varepsilon) \geq C\frac{\eta}{2}|\varepsilon|_F^2. \quad \square$$

Despite those strong properties of $\psi(\cdot, d)$ we note that $\psi(\varepsilon, d)$ is not even convex in d and ε together for any of the splittings considered below.

2.1.1. Isotropic splitting. In this model, any strain will lead to damage. The splitting is therefore

$$(6) \quad \psi_0^+(\varepsilon) = \psi_0(\varepsilon), \quad \psi_0^-(\varepsilon) = 0.$$

Without proof, we note the following simple properties of the energy density ψ defined by (5) and this splitting:

Lemma 2. The energy density ψ defined in (5) with the isotropic splitting (6) has the properties (P₁)–(P₅). Furthermore $\psi(\cdot, d)$ has the stronger property that it is in C^∞ and quadratic for all $d \in [0, 1]$.

2.1.2. Volumetric decompositions. The isotropic model is unphysical, because it produces fracturing for all kinds of strain. In [21], Lancioni and Royer-Carfagni obtained better results by letting only the deviatoric strain contribute to the degradation. They introduced the split

$$\psi_0^+(\varepsilon) = \psi_0(\text{dev } \varepsilon), \quad \psi_0^-(\varepsilon) = \psi_0(\text{vol } \varepsilon),$$

with the deviatoric–volumetric strain splitting

$$\text{vol } \varepsilon := \frac{\text{tr } \varepsilon}{m}I, \quad \text{dev } \varepsilon := \varepsilon - \text{vol } \varepsilon.$$

With these definition, the energies are

$$(7) \quad \psi_0^+(\varepsilon) = \left(\frac{\mu}{m} + \frac{\lambda}{2}\right)(\text{tr } \varepsilon)^2, \quad \psi_0^-(\varepsilon) = \mu\left(\varepsilon^2 - \frac{1}{m}(\text{tr } \varepsilon)^2\right) = \mu \text{dev } \varepsilon : \text{dev } \varepsilon.$$

Lemma 3. The energy density ψ defined in (5) with the isotropic volumetric splitting (7) has the properties (P₁)–(P₅). Furthermore $\psi(\cdot, d)$ has the stronger property that it is in C^∞ and quadratic for all $d \in [0, 1]$.

Proof. C^∞ -smoothness and thus (P₁) and (P₂) are straightforward. The fact that ψ_0^+ and ψ_0^- are quadratic, convex, and non-negative allows to derive (P₃), (P₄), and (P₅) from Lemma 1 and implies that $\psi(\cdot, d)$ is also quadratic. \square

The decomposition of Lancioni and Royer-Carfagni is still isotropic. Amor et al. [2] proposed to only degrade the expansive part of the volumetric strain. Using the ramp functions

$$\langle x \rangle_+ := \max\{0, x\}, \quad \langle x \rangle_- := \min\{0, x\}$$

that provide the decompositions $x = \langle x \rangle_+ + \langle x \rangle_-$ and $x^2 = \langle x \rangle_+^2 + \langle x \rangle_-^2$, they proposed the energy split

$$(8) \quad \psi_0^+(\boldsymbol{\varepsilon}) = \left(\frac{\mu}{m} + \frac{\lambda}{2}\right) \langle \text{tr } \boldsymbol{\varepsilon} \rangle_+^2, \quad \psi_0^-(\boldsymbol{\varepsilon}) = \left(\frac{\mu}{m} + \frac{\lambda}{2}\right) \langle \text{tr } \boldsymbol{\varepsilon} \rangle_-^2 + \mu \text{ dev } \boldsymbol{\varepsilon} : \text{ dev } \boldsymbol{\varepsilon},$$

where only the tensile volumetric strain contributes to damage.

Lemma 4. The energy density ψ defined in (5) with the anisotropic volumetric splitting (8) has the properties (P₁)–(P₅). Furthermore $\psi(\cdot, d)$ is not C^2 , unless $g(d) + k = 1$.

Proof. We first note that the squared ramp functions $\langle \cdot \rangle_{\pm}^2$ are convex, LC^1 with derivatives having a global Lipschitz constant 2, and piecewise C^2 (in the sense of [34, Definition 2.19]). Hence the functions ψ_0^{\pm} are also LC^1 with globally Lipschitz gradients and piecewise C^2 , which shows (P₁) and (using Lemma 1) (P₃). Being piecewise C^2 implies semismoothness (P₂) of $\nabla \psi(\cdot, d)$ [34, Proposition 2.26]. Noting that $\mu/m + \lambda/2 > 0$, convexity of the squared ramp functions furthermore implies that the functions ψ_0^{\pm} are also convex and non-negative, which by Lemma 1 provides (P₄) and (P₅).

For $g(d) + k = 1$ the functional $\psi(\cdot, d)$ is quadratic and thus C^2 . In the case $g(d) + k \neq 1$, if $\psi(\cdot, d)$ would be C^2 , then the function $t \mapsto \psi(tI, d)$ would also be C^2 . However, this function takes the form

$$\psi(tI, d) = \left(\frac{\mu}{m} + \frac{\lambda}{2}\right) m^2 t^2 \begin{cases} g(d) + k & \text{if } t \geq 0, \\ 1 & \text{if } t < 0 \end{cases}$$

and is thus piecewise quadratic but not C^2 in $t = 0$. □

2.1.3. Spectral decomposition. A more elaborate nonlinear splitting separating the tensile and compressive parts of the elastic energy was introduced in [24]. To define this splitting it is convenient to introduce the ordered eigenvalue function $\text{Eig} : \mathbb{S}^m \rightarrow \mathbb{R}^m$ on the space \mathbb{S}^m of symmetric $m \times m$ matrices, mapping any symmetric matrix M to the vector $\text{Eig}(M) \in \mathbb{R}^m$ containing its eigenvalues in ascending order. Using the ramp functions the tensile and compressive energies ψ_0^+ and ψ_0^- are then defined as

$$(9) \quad \psi_0^{\pm}(\boldsymbol{\varepsilon}) := \frac{\lambda}{2} \left\langle \sum_{i=1}^m \text{Eig}(\boldsymbol{\varepsilon})_i \right\rangle_{\pm}^2 + \mu \left[\sum_{i=1}^m \langle \text{Eig}(\boldsymbol{\varepsilon})_i \rangle_{\pm}^2 \right].$$

Note that this indeed defines a splitting $\psi_0 = \psi_0^+ + \psi_0^-$. For this splitting we will make the additional assumption that $\lambda \geq 0$.

To quantify the properties of $\psi(\boldsymbol{\varepsilon}, d)$ with respect to the strain tensor $\boldsymbol{\varepsilon}$ we use the theory of spectral functions. To this end we note that we can write ψ_0^{\pm} as

$$\psi_0^{\pm} = \widehat{\psi}_0^{\pm} \circ \text{Eig} : \mathbb{S}^m \rightarrow \mathbb{R}$$

with

$$\widehat{\psi}_0^\pm(\boldsymbol{\lambda}) := \frac{\lambda}{2} \left\langle \sum_{i=1}^m \lambda_i \right\rangle_\pm^2 + \mu \sum_{i=1}^m \langle \lambda_i \rangle_\pm^2.$$

The functions $\widehat{\psi}_0^\pm$ are *symmetric* in the sense that $\widehat{\psi}_0^\pm(\boldsymbol{\lambda})$ does not depend on the order of the entries of $\boldsymbol{\lambda} \in \mathbb{R}^m$. Having this form we can infer properties of the functions $\psi_0^\pm = \widehat{\psi}_0^\pm \circ \text{Eig}$ from properties of the symmetric functions $\widehat{\psi}_0^\pm$.

Lemma 5. Let $\lambda \geq 0$. Then the energy density ψ defined in (5) with the spectral splitting (9) has the properties (P₁)–(P₅). Furthermore $\psi(\cdot, d)$ is not C^2 , unless $g(d) + k = 1$.

Proof. We will first show (P₁)–(P₅). An essential ingredient is that the squared ramp functions $\langle \cdot \rangle_\pm^2$ are non-negative, piecewise quadratic, and convex.

(P₁) The squared ramp functions $\langle \cdot \rangle_\pm^2$ and thus $\widehat{\psi}_0^\pm$ are LC^1 . Now [27, Proposition 4.3] shows that the spectral functions $\psi_0^\pm = \widehat{\psi}_0^\pm \circ \text{Eig}$ are also LC^1 . Hence the same applies to $\psi(\cdot, d)$.

(P₂) The squared ramp functions $\langle \cdot \rangle_\pm^2$ are piecewise C^2 functions. Hence the gradients $\nabla \widehat{\psi}_0^\pm$ are piecewise C^1 functions (in the sense of [34, Definition 2.19]) and thus semismooth [34, Proposition 2.26]. Now [27, Proposition 4.5] provides semismoothness of $\nabla \psi_0^\pm$ and thus of $\nabla \psi(\cdot, d)$.

(P₃) Since the functions $\widehat{\psi}_0^\pm$ are piecewise quadratic and LC^1 the gradients $\nabla \widehat{\psi}_0^\pm$ are globally Lipschitz continuous. Now Corollary 43 of [3] provides global Lipschitz continuity of the gradients $\nabla \psi_0^\pm$ of the spectral functions ψ_0^\pm in the more general context of Euclidean Jordan algebras (which includes the special case of symmetric matrices). In fact, the Lipschitz constant of $\nabla \widehat{\psi}_0^\pm$ equals the one for $\nabla \psi_0^\pm$ if \mathbb{S}^m is equipped with the Frobenius norm. Using Lemma 1 this implies uniform Lipschitz continuity of $\psi(\cdot, d)$.

(P₄),(P₅) Since the functions $\widehat{\psi}_0^\pm$ are weighted sums of convex, non-negative squared ramp functions with nonnegative weights, they are convex and non-negative themselves. Convexity of the functions ψ_0^\pm then follows from [3, Theorem 41] while non-negativity of those functions is trivial. Now Lemma 1 provides (P₄) and (P₅).

To characterize second order differentiability of $\psi(\cdot, d)$ we first consider $g(d) + k = 1$. Then $\psi(\cdot, d)$ coincides with the quadratic function $\psi_0 = \psi_0^+ + \psi_0^-$ and is thus C^2 . In the case $g(d) + k \neq 1$, if $\psi(\cdot, d)$ would be C^2 , then the function $t \mapsto \psi(tE, d)$ for the fixed matrix E with $E_{ij} = \delta_{1i}\delta_{1j}$ would also be C^2 . However, this function takes the form

$$\psi(tE, d) = \left(\frac{\lambda}{2} + 1 \right) t^2 \begin{cases} g(d) + k & \text{if } t \geq 0, \\ 1 & \text{if } t < 0, \end{cases}$$

and is thus piecewise quadratic but not C^2 in $t = 0$. □

Remark 2.2. One can show that \mathbb{S}^m decomposes into finitely many disjoint subsets \mathcal{A}_i such that $\psi(\cdot, d)$ is twice continuously differentiable in the interior in each of these sets. A matrix $\boldsymbol{\varepsilon} \in \mathbb{S}^m$ is in the intersection of several $\overline{\mathcal{A}}_i$ if it either has an eigenvalue $\text{Eig}(\boldsymbol{\varepsilon})_i = 0$ or if $\text{tr } \boldsymbol{\varepsilon} = 0$. While $\nabla \psi(\cdot, d)$ is not differentiable at those points, there are still generalized second-order derivatives. For example, the generalized Jacobian in the sense of Clarke contains the derivatives of $\nabla \psi(\cdot, d)$ with respect to all the adjacent sets \mathcal{A}_i . Semismoothness essentially means that

such generalized derivatives provide an approximation that can be exploited in a generalized Newton method.

Remark 2.3. The additional assumption $\lambda \geq 0$ is essential for convexity of $\psi(\cdot, d)$. To see this we consider for $m = 2$ the line segment

$$\{D(t) = \text{diag}(-1, t) \mid t \in (0, 1)\} \subset \mathbb{S}^2.$$

Then, along this line segment, $\psi(\cdot, 1)$ is quadratic and takes the form

$$\psi(D(t), 1) = k\mu t^2 + \frac{\lambda}{2}(t-1)^2 + \mu = \left(k\mu + \frac{\lambda}{2}\right)t^2 - \lambda t + \frac{\lambda}{2} + \mu$$

which is strictly concave for $\lambda < 0$ and sufficiently small $k \ll 1$.

2.2. Crack surface density. The crack surface density function per unit volume of the solid is typically of the form [26]

$$\gamma(d, \nabla d) := c_\gamma \left(w(d) + \frac{w(1)}{c_l} l^2 |\nabla d|^2 \right),$$

with parameters c_γ , c_l , and l , and a parameter function $w : [0, 1] \rightarrow [0, 1]$. The internal length scale parameter l controls the size of the diffusive zone between a completely intact and a completely damaged material. For $l \rightarrow 0$ the regularized crack surface yields a sharp crack topology in the sense of Γ -convergence. For a given function w , the normalization constants c_γ and c_l must be chosen such that the integral of $\gamma(d, \nabla d)$ over the fractured domain converges to the surface measure of the crack set as $l \rightarrow 0$.

The function $w(d)$ models the local fracture energy. Two types of local crack density functions appear in the literature. Double well potentials (as briefly reviewed in [1]), provide an energy barrier between broken and unbroken state, but will be disregarded here. Instead, we focus on the two widely used functionals

$$w(d) = d, \quad c_l = \frac{1}{2}, \quad c_\gamma = \frac{3}{4\sqrt{2}l}$$

and

$$w(d) = d^2, \quad c_l = 1, \quad c_\gamma = \frac{1}{2l}.$$

They are referred to in the literature as Ambrosio–Tortorelli (AT) functionals of type 1 and 2, respectively.

Some authors like [20] prefer $w(d) = d^2$ because it has a local minimizer at $d = 0$. Thus, in the absence of mechanical strain, the unfractured solution $d \equiv 0$ is a minimizer of the total energy. As a result, no additional constraints need to be applied to ensure that $d \geq 0$. However, this argument becomes void when solver technology is available that can handle the explicit constraints $0 \leq d \leq 1$. In contrast, for the AT-1 functional we have $w' \neq 0$ in the intact state $d = 0$. Together with the constraint $d \in [0, 1]$ this leads to a threshold, i.e., a minimum load required to cause damage [26].

Kuhn et al. [20] proposed to regard the Ambrosio–Tortorelli functionals as special instances of the general family defined by

$$(10) \quad w(d) = (1 + \beta(1 - d))d$$

with $\beta \in [-1, 1]$. The Ambrosio–Tortorelli functionals are obtained by setting $\beta = 0$ for AT-1 and $\beta = -1$ for AT-2. Further choices of w are proposed in [26], which also do a detailed stability analysis for one-dimensional problems.

We note the following properties of the functional w in (10):

Lemma 6. The function w given in (10) has the following properties:

- (1) It fulfills $w(0) = 0$ and $w(1) = 1$.
- (2) It is strictly monotone increasing on $[0, 1]$ for all $\beta \in [-1, 1]$.
- (3) It is convex for all $\beta \leq 0$, and strictly convex for all $\beta < 0$.

For the rest of the paper we will assume the $w(\cdot)$ takes the form (10) with $\beta \leq 0$ such that $w(\cdot)$ is guaranteed to be convex and quadratic.

3. DISCRETIZATION AND THE ALGEBRAIC INCREMENT POTENTIAL

We use a fully implicit discretization in time, and Lagrange finite elements for discretization in space. Note that time discretizations using a local energy history field [23] are typically only semi-implicit (cf. Section 5.1). By using a fully implicit time discretization we retain the variational structure of the problem. Most of this chapter is spent investigating the properties of the increment functional.

3.1. Time discretization. It is shown in [25] that there is a natural time discretization for (1) that consists of sequences of minimization problems. Let the time interval $[0, T]$ be subdivided by time points t_n , $n = 0, 1, 2, \dots$. We obtain a time-discrete formulation by integrating the rate potential Π given in (4) along paths on $[t_n, t_{n+1}]$. Given initial values $(\mathbf{u}_n, d_n) \in \mathbf{H}_{\mathbf{u}_0} \times H_{d_0}$ at t_n , the continuous solution (\mathbf{u}, d) on this interval minimizes $\int_{t_n}^{t_{n+1}} \Pi(\dot{\mathbf{u}}, \dot{d}, \mathbf{u}, d) dt$ in the set of all paths of sufficient smoothness with $(\mathbf{u}(t_n), d(t_n)) = (\mathbf{u}_n, d_n)$ [25]. We then set $(\mathbf{u}_{n+1}, d_{n+1})$ to be $(\mathbf{u}(t_{n+1}), d(t_{n+1}))$. Defining $\mathcal{P}_n(\tilde{\mathbf{u}}, \tilde{d})$ as the set of suitably smooth paths in $\mathbf{H}_{\mathbf{u}_0} \times H_{d_0}$ from (\mathbf{u}_n, d_n) to $(\tilde{\mathbf{u}}, \tilde{d})$, and using that $\Pi(\dot{\mathbf{w}}, \dot{v}, \mathbf{w}, v) = \frac{d}{dt} \mathcal{E}(t, \mathbf{w}, v) + \mathcal{R}(v, \dot{v})$, this can be written as

$$\begin{aligned} (\mathbf{u}_{n+1}, d_{n+1}) &= \arg \min_{(\tilde{\mathbf{u}}, \tilde{d})} \left[\inf_{(\mathbf{w}, v) \in \mathcal{P}_n(\tilde{\mathbf{u}}, \tilde{d})} \int_{t_n}^{t_{n+1}} \left[\frac{d}{dt} \mathcal{E}(t, \mathbf{w}(t), v(t)) + \mathcal{R}(v(t), \dot{v}(t)) \right] dt \right] \\ &= \arg \min_{(\tilde{\mathbf{u}}, \tilde{d})} \left[\mathcal{E}(t_{n+1}, \tilde{\mathbf{u}}, \tilde{d}) - \mathcal{E}(t_n, \mathbf{u}_n, d_n) \right. \\ &\quad \left. + \inf_{(\mathbf{w}, v) \in \mathcal{P}_n(\tilde{\mathbf{u}}, \tilde{d})} \int_{t_n}^{t_{n+1}} \mathcal{R}(v(t), \dot{v}(t)) dt \right]. \end{aligned}$$

The last integral term is the length of $v : [t_n, t_{n+1}] \rightarrow H_{d_0}^1(\Omega)$ with respect to the Finsler norm given by \mathcal{R} . Minimizing over all paths gives the distance

$$\begin{aligned} \mathcal{D}(d_n, \tilde{d}) &:= \inf \left[\int_{t_n}^{t_{n+1}} \mathcal{R}(v(t), \dot{v}(t)) dt \right. \\ &\quad \left. : v \text{ is a sufficiently smooth path from } d_n \text{ to } \tilde{d} \right]. \end{aligned}$$

Then one step of the time discretization scheme is given by

$$(\mathbf{u}_{n+1}, d_{n+1}) := \arg \min_{(\mathbf{u}, d) \in \mathbf{H}_{\mathbf{u}_0}^1 \times H_{d_0}^1} \left[\mathcal{E}(t_{n+1}, \mathbf{u}, d) + \mathcal{D}(d_n, d) \right].$$

In our particular case (3), \mathcal{R} does not explicitly depend on d . The dissipation distance is then easily computed as [25, Example 3.2.5]

$$\mathcal{D}(v, w) = \mathcal{R}(w - v) = \int_{\Omega} I_{[0, \infty)}(w - v) dV = \int_{\Omega} I_{[v, \infty)}(w) dV.$$

We obtain the minimization problem

$$(11) \quad (\mathbf{u}_{n+1}, d_{n+1}) := \arg \min_{(\mathbf{u}, d) \in \mathbf{H}_{\mathbf{u}_0}^1 \times H_{d_0}^1} \Pi_{n+1}^\tau(\mathbf{u}, d),$$

with the increment potential

$$\Pi_{n+1}^\tau(\mathbf{u}, d) := \int_{\Omega} \psi(\boldsymbol{\varepsilon}(\mathbf{u}), d) dV + \int_{\Omega} g_c \gamma(d, \nabla d) dV + P_{\text{ext}}(t_{n+1}, \mathbf{u}) + \int_{\Omega} I_{[d_n, 1]}(d) dV.$$

Note that the time step size does not appear in this functional, because the model is rate-independent. Note also that the increment potential depends on the previous time step only through the indicator functional.

Lemma 7. Assume that $\Gamma_{D, \mathbf{u}}$ is non-trivial in the sense that its $m - 1$ -dimensional Hausdorff-measure is positive. Then the functional Π_{n+1}^τ is coercive on $\mathbf{H}_{\mathbf{u}_0}^1 \times H_{d_0}^1$.

Proof. Using the uniform coercivity (P₅) of $\psi(\cdot, d)$, $w(1) > 0$, and $w(d) \geq 0$ for $d \in [0, 1]$ we get

$$\int_{\Omega} \psi(\boldsymbol{\varepsilon}(\mathbf{u}), d) dV + \int_{\Omega} g_c \gamma(d, \nabla d) dV \geq C \int_{\Omega} |\boldsymbol{\varepsilon}(\mathbf{u})|_F^2 + |\nabla d|^2 dV$$

for some constant $C > 0$. Using Korn's inequality for \mathbf{u} , the Poincaré inequality for d , and the fact that $P_{\text{ext}}(t_{n+1}, \mathbf{u})$ grows at most linearly we get for another constant $C > 0$

$$\begin{aligned} \Pi_{n+1}^\tau(\mathbf{u}, d) &\geq C \left(\|\mathbf{u}\|_1^2 + \|d\|_1^2 - 1 - \left(\int_{\Omega} d dV \right)^2 \right) + \int_{\Omega} I_{[d_n, 1]}(d) dV \\ &\geq C \left(\|\mathbf{u}\|_1^2 + \|d\|_1^2 - 1 - |\Omega|^2 \right), \end{aligned}$$

where we have used that the constraint $d \in [0, 1]$ implies $|\int_{\Omega} d dV| \leq |\Omega|$ in the second inequality. \square

Lemma 8. The functional Π_{n+1}^τ is weakly lower semicontinuous on $\mathbf{H}_{\mathbf{u}_0}^1 \times H_{d_0}^1$.

Proof. Since weak lower semicontinuity of the other terms in Π_{n+1}^τ follows from convexity and lower semicontinuity of the integrands, we only need to consider the non-convex term

$$(12) \quad \int_{\Omega} \psi(\boldsymbol{\varepsilon}(\mathbf{u}), d) + I_{[d_n, 1]}(d) dV.$$

To this end we note that (12) can be written as $J(\mathbf{u}, d, \nabla \mathbf{u})$ for

$$J(\mathbf{u}, d, \xi) := \int_{\Omega} F(x, (\mathbf{u}(x), d(x)), \xi) dV$$

and the density $F : \Omega \times (\mathbb{R}^m \times \mathbb{R}) \times \mathbb{R}^{m \times m} \rightarrow \mathbb{R} \cup \{\infty\}$ given by

$$F(x, (\mathbf{u}, d), \xi) = \psi\left(\frac{1}{2}(\xi + \xi^T), d\right) + I_{[d_n, 1]}(d).$$

Since F is a Carathéodory function, non-negative (and thus uniformly bounded from below), and convex in ξ for all $(x, (\mathbf{u}, d)) \in \Omega \times (\mathbb{R}^m \times \mathbb{R})$, it satisfies the assumptions of Theorem 3.4 in [8].

Now let $(\mathbf{u}^\nu, d^\nu) \rightharpoonup (\mathbf{u}, d)$ be a weakly convergent sequence in $\mathbf{H}_{\mathbf{u}_0}^1 \times H_{d_0}^1$. Then, by the compactness of the embedding into $L^2(\Omega, \mathbb{R}^m \times \mathbb{R})$ we get

$$(\mathbf{u}^\nu, d^\nu) \rightarrow (\mathbf{u}, d) \quad \text{in } L^2(\Omega, \mathbb{R}^m \times \mathbb{R}).$$

Furthermore, the $H^1(\Omega, \mathbb{R}^m \times \mathbb{R})$ -weak convergence of (\mathbf{u}^ν, d^ν) implies $L^2(\Omega, \mathbb{R}^{m \times m})$ -weak convergence of $\nabla \mathbf{u}^\nu$

$$\xi^\nu := \nabla \mathbf{u}^\nu \rightharpoonup \nabla \mathbf{u} =: \xi \quad \text{in } L^2(\Omega, \mathbb{R}^{m \times m}),$$

because $(\mathbf{u}, d) \mapsto \eta(\nabla \mathbf{u})$ is in $H^1(\Omega, \mathbb{R}^m \times \mathbb{R})'$ for each $\eta \in L^2(\Omega, \mathbb{R}^{m \times m})'$. Now Theorem 3.4 of [8] provides

$$\liminf_{\nu \rightarrow \infty} J(\mathbf{u}^\nu, d^\nu, \xi^\nu) \geq J(\mathbf{u}, d, \xi) = J(\mathbf{u}, d, \nabla \mathbf{u}). \quad \square$$

As a direct consequence of coercivity and weak lower semicontinuity we get existence of a minimizer of the increment functional:

Theorem 3.1. *There is a solution to the minimization problem (11), i.e., there exists a global minimizer $(\mathbf{u}_{n+1}, d_{n+1}) \in \mathbf{H}_{\mathbf{u}_0}^1 \times H_{d_0}^1$ of Π_{n+1}^τ .*

3.2. Finite element discretization. The increment problem (11) of the previous section is posed on the pair of spaces $\mathbf{H}_{\mathbf{u}_0}^1$ for the displacements and $H_{d_0}^1$ for the damage variable. Let \mathcal{G} be a conforming finite element grid for Ω . We discretize the function spaces by standard first-order Lagrangian finite elements. In order to derive an algebraic form of the discretized increment functional we make use of the standard scalar nodal basis $\{\theta_i\}_{i=1}^M$ associated to the grid nodes $\{p_1, \dots, p_M\} =: \mathcal{N} \subset \Omega$. Identifying the \mathbb{R}^m -valued and scalar finite element functions \mathbf{u} and d with their coefficient vectors $\mathbf{u} \in \mathbb{R}^{M, m}$ and $d \in \mathbb{R}^M$, respectively, we write

$$\mathbf{u}_j = \sum_{i=1}^M u_{i,j} \theta_i, \quad d = \sum_{i=1}^M d_i \theta_i,$$

where $u_{i,j} = \mathbf{u}_j(p_i)$ and $d_i = d(p_i)$. For the integration we use two kinds of quadrature rules: Integrals of smooth nonlinear terms over a grid element e are approximated using a higher-order quadrature rule $\int_{e,h}$, while the integral over the nonsmooth term $I_{[d_n, 1]}(d)$ is approximated using the grid nodes p_i as quadrature point, which is often referred to as *lumping*. Using these approximations we obtain the algebraic increment functional $\mathcal{J} := \Pi_{n+1}^{\tau, \mathcal{G}}$ given by

$$(13) \quad \mathcal{J}(\mathbf{u}, d) := \underbrace{\int_{\Omega, h} (\psi(\boldsymbol{\varepsilon}(\mathbf{u}), d)) dV + \int_{\Omega} g_c \gamma(d, \nabla d) + P_{\text{ext}}(t_{n+1}, \mathbf{u})}_{=: \mathcal{J}_0(\mathbf{u}, d)} + \underbrace{\sum_{i=1}^M I_{[d_n(p_i), 1]}(d_i)}_{=: \varphi(d)}.$$

Here the quadrature rule $\int_{\Omega, h}(\cdot) dV$ is given by

$$\int_{\Omega, h} f dV = \sum_{e \in \mathcal{G}} \int_{e, h} f dV, \quad \int_{e, h} f = \sum_{\alpha=1}^{\alpha_{\max}} f(q_{e, \alpha}) \omega_{e, \alpha}$$

with positive weights $\omega_{e, \alpha}$. Notice that we do not need quadrature weights in the last term of \mathcal{J} , because the indicator function only takes values in $\{0, \infty\}$.

To highlight the algebraic structure of \mathcal{J} we introduce the linear operator $\mathcal{L} : (\mathbb{R}^{M, m} \times \mathbb{R}^M) \rightarrow ((\mathbb{S}^m \times \mathbb{R})^{\alpha_{\max}})^{\mathcal{G}}$ with

$$\mathcal{L}(\mathbf{u}, d)_{e, \alpha} := ((\boldsymbol{\varepsilon}(\mathbf{u}))(q_{e, \alpha}), d(q_{e, \alpha})) \quad \alpha = 1, \dots, \alpha_{\max}, e \in \mathcal{G}.$$

Then the first part \mathcal{J}_0 of the functional can be written as

$$\mathcal{J}_0(\mathbf{u}, d) = \underbrace{\sum_{e \in \mathcal{G}} \sum_{\alpha=1}^{\alpha_{\max}} \psi(\mathcal{L}(\mathbf{u}, d)_{e,\alpha}) \omega_{e,\alpha}}_{=:A(\mathbf{u},d)} + \underbrace{\int_{\Omega} g_c \gamma(d, \nabla d) + P_{\text{ext}}(t_{n+1}, \mathbf{u})}_{=:B(\mathbf{u},d)}.$$

Notice that for the price of a more complex index notation, the linear operator \mathcal{L} can also be written as a sparse matrix with suitable blocking structure. In this case $\mathcal{L}(\cdot, \cdot)_{e,\alpha} : (\mathbb{R}^{M,m} \times \mathbb{R}^M) \rightarrow (\mathbb{S}^m \times \mathbb{R})$ corresponds to the (e, α) -th sparse row of this matrix.

As an approximation of the boundary conditions from $\mathbf{H}_{\mathbf{u}_0}^1 \times H_{d_0}^1$ we will consider \mathcal{J} on the affine subspace $H^{\text{alg}} = H_{\mathbf{u}_0}^{\text{alg}} \times H_{d_0}^{\text{alg}}$ where

$$\begin{aligned} H_{\mathbf{u}_0}^{\text{alg}} &= \{\mathbf{u} \in \mathbb{R}^{M,m} \mid \mathbf{u}(p) = \mathbf{u}_0(p) \quad \forall p \in \mathcal{N} \cap \Gamma_{D,\mathbf{u}}\}, \\ H_{d_0}^{\text{alg}} &= \{d \in \mathbb{R}^M \mid d(p) = d_0(p) \quad \forall p \in \mathcal{N} \cap \Gamma_{D,d}\}. \end{aligned}$$

The associated homogeneous subspace is denoted by H_0^{alg} . In the following we make the assumption that $\mathcal{N} \cap \Gamma_{D,\mathbf{u}}$ is rich enough to ensure a discrete Korn inequality such that $\|\boldsymbol{\varepsilon}(\mathbf{u})\|_0 \geq C \|\mathbf{u}\|_1$ holds for all $\mathbf{u} \in H_{\mathbf{u}_0}^{\text{alg}}$. Furthermore we introduce the discrete feasible set

$$\mathcal{K}^{\text{alg}} = H_{\mathbf{u}_0}^{\text{alg}} \times \left(H_{d_0}^{\text{alg}} \cap \mathcal{K}_d^{\text{alg}} \right), \quad \mathcal{K}_d^{\text{alg}} = \prod_{i=1}^M [d_n(p_i), 1]$$

that additionally incorporates the pointwise irreversibility constraints.

3.3. Properties of the discrete incremental potential. The convergence property of the TNNMG algorithm heavily rely on the algebraic structure of the problem. Hence we now collect the essential structural properties of the algebraic increment functional \mathcal{J} . While stronger properties hold true for some splittings of ψ , we only note the necessary properties shared by all of the proposed splittings. In order to preserve the significant properties in the presence of numerical quadrature, we assume that quadrature rule $\int_{e,h} f$ can at least integrate the isotropic energy $f = |\boldsymbol{\varepsilon}(\mathbf{u})|_F^2$ exactly for any finite element function \mathbf{u} .

Lemma 9. The functional $\mathcal{J}_0 = A + B$ has the following properties:

- (1) $\mathcal{J}_0(\cdot, d) \in LC^1$ and $\mathcal{J}_0(\mathbf{u}, \cdot) \in C^2$ for any $d \in \mathcal{K}_d^{\text{alg}}$ and $\mathbf{u} \in \mathbb{R}^{M,m}$.
- (2) The gradient $\nabla \mathcal{J}_0(\cdot, d)$ is semismooth.
- (3) The gradient $\nabla \mathcal{J}_0(\cdot, d)$ is globally Lipschitz continuous uniformly in d .
- (4) $\mathcal{J}_0(\cdot, d)$ is strongly convex uniformly in d on $H_{\mathbf{u}_0}^{\text{alg}}$.
- (5) $\mathcal{J}_0(\mathbf{u}, \cdot)$ is convex on $\mathcal{K}_d^{\text{alg}}$.

Proof. The smoothness properties, uniform global Lipschitz continuity, and convexity follow from the corresponding properties of ψ and γ , and from linearity of \mathcal{L} .

To see uniform strong convexity, we note that uniform strong convexity of $\psi(\cdot, d)$ implies that there is some $\eta > 0$ such that $\phi(\boldsymbol{\varepsilon}, d) = \psi(\boldsymbol{\varepsilon}, d) - \frac{\eta}{2} |\boldsymbol{\varepsilon}|_F^2$ is convex. Using the exactness assumption on the quadrature rule we get

$$\sum_{e \in \mathcal{G}} \sum_{\alpha=1}^{\alpha_{\max}} \phi(\mathcal{L}(\mathbf{u}, d)_{e,\alpha}) \omega_{e,\alpha} = A(\mathbf{u}, d) - \frac{\eta}{2} \|\boldsymbol{\varepsilon}(\mathbf{u})\|_0^2.$$

Since this is a weighted sum of convex functions $\phi(\cdot, d(q_{e,\alpha}))$ with positive weights $\omega_{e,\alpha}$, it is itself convex with respect to \mathbf{u} . Thus $A(\mathbf{u}, d)$ is the sum of a convex function and the function $\|\boldsymbol{\varepsilon}(\mathbf{u})\|_0^2$. Since the latter is strongly convex on $H_{\mathbf{u}_0}^{\text{alg}}$ independently of d , the same applies to $A(\mathbf{u}, d)$ and $(A+B)(\cdot, d)$.

Finally we note that convexity of g and γ imply convexity of $(A+B)(\mathbf{u}, \cdot)$. \square

The TNNMG algorithm is based on a crucial property called block-separability, which states that the nonsmooth part of the objective functional can be written as a sum, such that the sets of independent variables of the addend functionals are disjoint. We note that $\mathcal{J} = \mathcal{J}_0 + \varphi$ is of the desired form with a smooth part $\mathcal{J}_0 = A+B$ and a block-separable nonsmooth part

$$(14) \quad \varphi(d) := \sum_{i=1}^M \varphi_i(d_i), \quad \varphi_i(\xi) := I_{[d_n(p_i), 1]}(\xi),$$

which can also be written as the indicator functional $\varphi(d) = I_{\mathcal{K}_d^{\text{alg}}}(d)$ of the feasible set $\mathcal{K}_d^{\text{alg}}$ of the $n+1$ -th time step.

Due to the nonsmoothness of φ , the smoothness properties of \mathcal{J}_0 do obviously not carry over to the full functional \mathcal{J} . Furthermore \mathcal{J} is in general not convex as a whole. However we still have the following:

Lemma 10. The functional \mathcal{J} is proper, lower semicontinuous, and coercive on H^{alg} . Furthermore it is convex in \mathbf{u} and convex in d .

Proof. Being the indicator function of the closed, nonempty, convex set $\mathcal{K}_d^{\text{alg}}$ it is clear that the separable nonsmooth functional φ is convex, proper, and lower semicontinuous. Combining this with smoothness of \mathcal{J}_0 we get that \mathcal{J} is proper and lower semicontinuous. Similarly, convexity in \mathbf{u} and d follows from the corresponding properties of \mathcal{J}_0 and φ .

Using the uniform coercivity (P₅) of $\psi(\cdot, d)$, $w(1) > 0$, and $w(d) \geq 0$ (as in the proof of Lemma 7) and the exactness assumption on the quadrature rule (as in the proof of Lemma 9) we get

$$A(\mathbf{u}, d) + B(\mathbf{u}, d) - P_{\text{ext}}(t_{n+1}, \mathbf{u}) \geq C \int_{\Omega} |\boldsymbol{\varepsilon}(\mathbf{u})|_F^2 + |\nabla d|^2 dV$$

for some constant $C > 0$. Now we can proceed as in the proof of Lemma 7 to show coercivity of \mathcal{J} . \square

4. TRUNCATED NONSMOOTH NEWTON MULTIGRID FOR BRITTLE FRACTURE

The Truncated Nonsmooth Newton Multigrid method (TNNMG) is designed to solve nonsmooth block-separable minimization problems on Euclidean spaces. In a nutshell, one step of the TNNMG method consists of a nonlinear Gauß–Seidel-type smoother and a subsequent inexact Newton-type correction in a constrained subspace. The nonlinear smoother computes local corrections by subsequent (possibly inexact) solving of reduced minimization problems in small subspaces. As the nonlinear smoother is responsible for ensuring convergence, while the Newton corrections accelerate the convergence, the ingredients of the nonlinear smoother have to be selected carefully.

It is a well known result [12] that nonlinear Gauß–Seidel-type methods can easily get stuck, if the subspace decomposition used to construct localized minimization problems is not aligned with the decomposition induced by the block-separable

nonsmooth term. In our case, the nonsmooth term φ is separable with respect to the decomposition of unknowns induced by the grid vertices. An additional requirement is that the local minimization problems must be uniquely solvable, which is typically ensured by choosing the decomposition such that the local problems are strictly convex.

In view of these requirements we first decompose the space according to the grid vertices and then with respect to the local \mathbf{u} - and d -degrees of freedom leading to a decomposition

$$(15) \quad \mathbb{R}^{M,m} \times \mathbb{R}^M = (\mathbb{R}^m \times \mathbb{R})^M = \sum_{j=1}^M (V_{j,\mathbf{u}} + V_{j,d}).$$

Here the m -dimensional subspace $V_{j,\mathbf{u}}$ represents the displacement components at the j -th grid vertex, while the one-dimensional subspace $V_{j,d}$ represents the d -components at this vertex. All other components are set to zero in these spaces which allows to translate the decomposition from a product to a direct sum. For simplicity we use a plain enumeration of these subspaces in alternating order

$$(16) \quad V_{2j-1} = V_{j,\mathbf{u}}, \quad V_{2j} = V_{j,d}, \quad j = 1, \dots, M.$$

Notice that with this splitting none of the nonsmooth terms φ_i in (14) couples across different subspaces. Furthermore, by Lemma 9 the restriction of \mathcal{J} to any affine subspace $(\mathbf{u}, d) + V_i$, $i = 1, \dots, 2M$ is convex.

We will now introduce the TNNMG method. For simplicity we first assume that $\Gamma_{D,\mathbf{u}}$ and $\Gamma_{D,d}$ are empty and that \mathcal{J}_0 is C^2 . Let $\nu \in \mathbb{N}_0$ denote the iteration number. Given a previous iterate $\mathbf{U}^\nu = (\mathbf{u}, d)^\nu \in \mathbb{R}^{M,m} \times \mathbb{R}^M$, one iteration of the TNNMG method consists of the following four steps:

(1) **Nonlinear presmoothing**

- (a) Set $\mathbf{W}^0 = \mathbf{U}^\nu$
- (b) For $i = 1, \dots, 2M$ compute $\mathbf{W}^i \in \mathbf{W}^{i-1} + V_i$ as

$$(17) \quad \mathbf{W}^i \approx \arg \min_{\mathbf{w} \in \mathbf{W}^{i-1} + V_i} \mathcal{J}(\mathbf{W})$$

- (c) Set $\mathbf{U}^{\nu+\frac{1}{2}} = \mathbf{W}^{2M}$

(2) **Inexact linear correction**

- (a) Determine the maximal subspace $W_\nu \subset \mathbb{R}^{M,m} \times \mathbb{R}^M$ such that the restriction $\mathcal{J}|_{W_\nu}$ is C^2 at $\mathbf{U}^{\nu+\frac{1}{2}}$
- (b) Compute $c^\nu \in W_\nu$ as an inexact Newton step on W_ν

$$(18) \quad c^\nu \approx -(\mathcal{J}''(\mathbf{U}^{\nu+\frac{1}{2}})|_{W_\nu \times W_\nu})^{-1}(\mathcal{J}'(\mathbf{U}^{\nu+\frac{1}{2}})|_{W_\nu})$$

(3) **Projection**

Compute the Euclidean projection $c_{\text{pr}}^\nu = P_{\text{dom } \mathcal{J}} - \mathbf{U}^{\nu+1/2}(c^\nu)$, i.e., choose c_{pr}^ν such that $\mathbf{U}^{\nu+\frac{1}{2}} + c_{\text{pr}}^\nu$ is closest to $\mathbf{U}^{\nu+\frac{1}{2}} + c^\nu$ in $\text{dom } \mathcal{J}$

(4) **Damped update**

- (a) Compute a $\rho_\nu \in [0, \infty)$ such that $\mathcal{J}(\mathbf{U}^{\nu+\frac{1}{2}} + \rho_\nu c_{\text{pr}}^\nu) \leq \mathcal{J}(\mathbf{U}^{\nu+\frac{1}{2}})$
- (b) Set $(\mathbf{u}, d)^{\nu+1} = \mathbf{U}^{\nu+1} = \mathbf{U}^{\nu+\frac{1}{2}} + \rho_\nu c_{\text{pr}}^\nu$

The algorithm is easily generalized to non-trivial Dirichlet boundary conditions by leaving out all subspaces associated to Dirichlet vertices during the nonlinear smoothing, and by additionally requiring $W_\nu \subset H_0^{\text{alg}}$ for the coarse correction subspace. Then, if the initial iterate satisfies the boundary conditions, i.e., if $(\mathbf{u}_d)^0 \in H^{\text{alg}}$, the method will only iterate within this affine subspace, which preserves the Dirichlet boundary conditions for all iterates.

The canonical choice for the linear correction step (18) is a single linear multigrid step, which explains why the overall method is classified as a multigrid method. If a grid hierarchy is available, then a geometric multigrid method is preferable. Otherwise, a suitable constructed algebraic multigrid step for small-strain elasticity problems will work just as well. Section 4.1 will discuss convergence of the method based on an abstract convergence theory. The abstract theory will be used as a guideline for the discussion of nonlinear smoothers in Sections 4.2. Finally 4.3 will discuss the linear coarse correction in more detail.

4.1. Convergence results. The TNNMG method was originally introduced for convex problems where global convergence to global minimizers can be shown [13, 14, 16] These classical results cannot be applied here, due to the non-convexity of \mathcal{J} . As a generalization of previous results, [15] introduced an abstract convergence theory that also covers non-convex problems. In the following we will summarize some results from this work. These will later be used as a guideline for specifying how to solve the local subproblems (17) and the coarse correction problem (18). In order to simplify the presentation some of the terminology and notation used in [15] is avoided in favor of a more specific notation adjusted to the algorithm as introduced above.

Theorem 4.1. *Let $\mathcal{J} : \mathbb{R}^L \rightarrow \mathbb{R} \cup \{\infty\}$ be coercive, proper, lower semicontinuous, and continuous on its domain, and assume that $\mathcal{J}(\mathbf{V} + (\cdot))$ has a unique global minimizer in V_i for all i and each $\mathbf{V} \in \text{dom } \mathcal{J}$. Assume that the inexact local corrections \mathbf{W}^i are given by $\mathbf{W}^i = \mathcal{M}_i(\mathbf{W}^{i-1})$ for local correction operators*

$$\mathcal{M}_i : \text{dom } \mathcal{J} \rightarrow \text{dom } \mathcal{J}, \quad \mathcal{M}_i - \text{Id} : \text{dom } \mathcal{J} \rightarrow V_i$$

having the properties:

- (1) *Monotonicity:* $\mathcal{J}(\mathcal{M}_i(\mathbf{V})) \leq \mathcal{J}(\mathbf{V})$ for all $\mathbf{V} \in \text{dom } \mathcal{J}$.
- (2) *Continuity:* $\mathcal{J} \circ \mathcal{M}_i$ is continuous.
- (3) *Stability:* $\mathcal{J}(\mathcal{M}_i(\mathbf{V})) < \mathcal{J}(\mathbf{V})$ if $\mathcal{J}(\mathbf{V})$ is not minimal in $\mathbf{V} + V_i$.

Furthermore assume that the initial iterate is feasible, i.e., $\mathbf{U}^0 \in \text{dom } \mathcal{J}$, and that the coarse correction is monotone, i.e. $\mathcal{J}(\mathbf{U}^{\nu+1}) \leq \mathcal{J}(\mathbf{U}^{\nu+\frac{1}{2}})$. Then any accumulation point \mathbf{U} of (\mathbf{U}^ν) is stationary in the sense that

$$(19) \quad \mathcal{J}(\mathbf{U}) \leq \mathcal{J}(\mathbf{U} + \mathbf{V}) \quad \forall \mathbf{V} \in V_i, \quad \forall i.$$

Proof. This is Theorem 4.1 in [15]. □

Now we discuss the application of this theorem to the phase-field brittle-fracture problem. First we interpret the stationarity result.

Proposition 1. Let \mathcal{J} be given by (13) and the subspaces V_i by (15) and (16). Then any stationary point \mathbf{U} in the sense of (19) is first-order optimal in the sense of

$$\langle \nabla \mathcal{J}_0(\mathbf{U}), \mathbf{W} - \mathbf{U} \rangle \leq 0 \quad \forall \mathbf{W} \in \text{dom } \mathcal{J}.$$

Proof. The stationarity (19) implies the variational inequalities

$$\langle \nabla \mathcal{J}_0(\mathbf{U}), \mathbf{W}_i - \mathbf{U} \rangle \leq 0 \quad \forall \mathbf{W}_i \in \text{dom } \mathcal{J} \cap (\mathbf{U} + V_i)$$

for each subspace V_i . Now let $\mathbf{W} \in \text{dom } \mathcal{J}$. Since the splitting (15) is direct one can split \mathbf{W} uniquely into

$$\mathbf{W} = \mathbf{U} + \sum_{i=1}^{2M} \mathbf{V}_i, \quad \mathbf{V}_i \in V_i.$$

Using the product structure of $\text{dom } \mathcal{J}$ we find that $\mathbf{W}_i := \mathbf{U} + \mathbf{V}_i \in \text{dom } \mathcal{J} \cap (\mathbf{U} + V_i)$. Summing up the variational inequalities for those \mathbf{W}_i we obtain the assertion. \square

Next we investigate the assumptions of the theorem. First we note that \mathcal{J} as given in (13) is coercive, proper, and lower semicontinuous by Lemma 10. Furthermore, \mathcal{J}_0 is continuous and the indicator function φ is continuous on its domain. Hence the latter is also true for $\mathcal{J} = \mathcal{J}_0 + \varphi$. Subspaces V_i with odd index i only vary in $\mathbf{u}(p_i)$ such that existence of a unique minimizer of $\mathcal{J}(\mathbf{W} + (\cdot))|_{V_i}$ follows from the strong convexity of $\mathcal{J}(\cdot, d)$ shown in Lemma 9. For even i these subspaces are associated to nodal damage degrees of freedom $d(p_i)$. Although $\mathcal{J}(\mathbf{u}, \cdot)$ is in general only convex, but not strictly convex, the restriction $\mathcal{J}(\mathbf{W} + (\cdot))|_{V_i}$ to a single node is a strictly convex quadratic functional, which again implies existence of a unique minimizer. Finally the monotonicity $\mathcal{J}(\mathbf{U}^{\nu+1}) \leq \mathcal{J}(\mathbf{U}^{\nu+\frac{1}{2}})$ of the coarse correction is a direct consequence of the damped update.

It remains to identify proper local correction operators \mathcal{M}_i satisfying the above assumptions. As a first result we show that solving the local minimization problems (17) exactly leads to a convergent algorithm in the above given sense.

Lemma 11. Let \mathcal{J} be given by (13) and the subspaces V_i by (15) and (16). Then the exact local solution operators

$$\mathcal{M}_i(\mathbf{W}) := \arg \min_{\mathbf{V} \in \mathbf{W} + V_i} \mathcal{J}(\mathbf{V})$$

satisfy the assumptions of Theorem 4.1.

Proof. This is Lemma 5.1 in [15]. \square

Depending on the damaged energy density ψ , solving the restricted problems exactly may not be practical. As a remedy, it is also shown in [15] that inexact minimization is sufficient as long as it guarantees sufficient decrease of the energy. In fact we do not need $\mathbf{W}^i = \mathcal{M}_i(\mathbf{W}^{i-1})$ exactly but may relax this to $\mathcal{J}(\mathbf{W}^i) \leq \mathcal{J}(\mathcal{M}_i(\mathbf{W}^{i-1}))$ for a suitable continuous \mathcal{M}_i . However, sufficient decrease is in general hard to check rigorously. In the following we cite one inexact variant from [15] where sufficient descent is guaranteed a priori.

Lemma 12. Let \mathcal{J} be given by (13) and the subspaces V_i by (15) and (16). For each subspace V_i let C_i be a symmetric positive definite matrix that satisfies

$$\langle \nabla \mathcal{J}_0(\mathbf{W} + \mathbf{V}) - \nabla \mathcal{J}_0(\mathbf{W}), \mathbf{V} \rangle \leq \langle C_i \mathbf{V}, \mathbf{V} \rangle \quad \forall \mathbf{W} \in \text{dom } \mathcal{J}, \mathbf{V} \in V_i.$$

Then the correction operators

$$\begin{aligned} \mathcal{M}_i(\mathbf{W}) := \arg \min_{\mathbf{V} \in (\mathbf{W} + V_i) \cap \text{dom } \mathcal{J}} & \mathcal{J}(\mathbf{W}) + \langle \nabla \mathcal{J}_0(\mathbf{W}), \mathbf{V} - \mathbf{W} \rangle \\ & + \frac{1}{2} \langle C_i(\mathbf{V} - \mathbf{W}), \mathbf{V} - \mathbf{W} \rangle \end{aligned}$$

satisfy the assumptions of Theorem 4.1.

Proof. This is Lemma 5.8 in [15]. \square

4.2. Smoothers for brittle fracture problems. The smoother of the TNNMG method performs a sequence of (inexact) minimization problems in low-dimensional subspaces V_i . Different approaches are possible here, implementing different compromises between convergence speed, wall-time per iteration, and ease of programming. As there are two types of degrees of freedom, two types of solvers are needed as well.

4.2.1. Subspaces of displacement degrees of freedom. We first consider the subspaces $V_i = V_{(i+1)/2, \mathbf{u}}$ for odd i spanned by the m displacement degrees of freedom at the vertex $p_{(i+1)/2}$. Noting that elements of this subspace only vary in the displacement component, the minimization problem (17) is equivalent to

$$(20) \quad \arg \min_{(\mathbf{v}, 0) \in V_i} L_i(\mathbf{v}).$$

Here, the restricted functional $L_i(\mathbf{v}) = \mathcal{J}(\mathbf{W}^{i-1} + (\mathbf{v}, 0))$ takes the form

$$(21) \quad L_i(\mathbf{v}) = \int_{\Omega, h} (g(d) + k)\psi_0^+(\boldsymbol{\varepsilon}(\mathbf{u} + \mathbf{v})) + \psi_0^-(\boldsymbol{\varepsilon}(\mathbf{u} + \mathbf{v})) dV + P_{\text{ext}}(t_{n+1}, \mathbf{v}) + \text{const},$$

where we have used $(\mathbf{u}, d) = \mathbf{W}^{i-1}$. The precise nature of L_i depends on the type of energy split used by the model. If the isotropic splits (6) or (7) are used, (21) is a strictly convex quadratic functional on a vector space, and can be minimized exactly by solving an $m \times m$ system of linear equations.

For the anisotropic splittings (8) and (9), the functional is still strictly convex and once continuously differentiable. The classical Hesse matrix, however, is not guaranteed to exist. However, by Lemma 9, the increment functional is semismooth. This suggests various natural choices for local solvers, such as steepest-descent methods or nonsmooth Newton methods [34]. When these are used to solve the local problems (17) exactly, global convergence of the overall TNNMG method follows from Theorem 4.1 and Lemma 11 above.

However, as mentioned in the previous section, Theorem 4.1 is more general, and also shows convergence for certain types of inexact local solvers (such as the one in Lemma 12). Such a setup can make iterations much faster, while keeping the corresponding deterioration of the convergence rate within acceptable limits. Possible approaches are:

- One Newton step with the smooth part replaced by a quadratic upper bound $(1 + k)\psi_0''$,
- One (or another fixed number of) semismooth Newton steps,
- One gradient step with exact line search.

For the first variant, global convergence of the TNNMG solver follows from Lemma 12. For the other two, the problem of showing convergence is open. Section 5 will show how some of these choices fare in practice.

4.2.2. *Subspaces spanned by damage degrees of freedom.* For subspaces $V_i = V_{i/2,d}$ with even i , i.e., subspaces spanned by the damage degree of freedom at the vertex $p_{i/2}$, the minimization problem (17) is equivalent to

$$\arg \min_{(0,v) \in V_i} L_i(v),$$

with a restricted functional $L_i(v) := \mathcal{J}(\mathbf{W}^{i-1} + (0,v))$. For all choices of damage functions g described in Section 2 this is a strictly convex quadratic functional on a closed interval, whose minimizer can be computed directly. We therefore always assume that these problems are solved exactly.

4.3. **Linear multigrid corrections.** For the linear correction step (18) we need to compute a constrained Newton-type correction

$$c^\nu \approx -(\mathcal{J}''(\mathbf{U}^{\nu+\frac{1}{2}})|_{W_\nu \times W_\nu})^{-1}(\mathcal{J}'(\mathbf{U}^{\nu+\frac{1}{2}})|_{W_\nu})$$

at least inexactly. This requires to determine the subspace W_ν , the constrained first- and second-order derivatives $\mathcal{J}'(\mathbf{U}^{\nu+\frac{1}{2}})|_{W_\nu}$ and $\mathcal{J}''(\mathbf{U}^{\nu+\frac{1}{2}})|_{W_\nu \times W_\nu}$ on this subspace, and finally to solve the system inexactly.

It is easy to see that the largest subspace W_ν where \mathcal{J} is differentiable in a neighborhood of $\mathbf{U}^{\nu+\frac{1}{2}} = (\mathbf{u}^{\nu+\frac{1}{2}}, d^{\nu+\frac{1}{2}})$ is given by

$$W_\nu = \left\{ \mathbf{U} = (\mathbf{u}, d) \mid d_i = 0 \text{ if } (d^{\nu+\frac{1}{2}})_i \notin (d_n(p_i), 1) \right\}.$$

In this subspace the nonsmooth indicator functional φ is identical to zero such that we only need to compute first- and second-order derivatives of the smooth part \mathcal{J}_0 , which are then constrained to the degrees of freedom which are allowed to be nonzero in W_ν . This can easily be achieved by setting rows and columns to zero for degrees of freedom not contained in W_ν . For all splittings where the degraded density ψ is not C^2 , it is at least locally Lipschitz and semi-smooth. In this case a generalized second-order derivative $\mathcal{J}_0''(\mathbf{U}^{\nu+\frac{1}{2}})$ can be used as a replacement of the classical Hesse matrix making (18) a semi-smooth Newton step. For the inexact solution one step of a classical linear multigrid method can be used. Here we only need to take care that the linear smoother can deal with the non-trivial kernel resulting from constraining the linearization. For a linear Gauß–Seidel smoother this amounts to omitting corrections for rows with zero diagonal entry.

5. NUMERICAL EXAMPLES

In this last section we demonstrate the speed and robustness of the TNNMG solver with two numerical examples. For both of them we study four instances from the family of models discussed in this manuscript: the isotropic and the spectral splittings ((6) and (9), respectively), combined with the AT-1 and AT-2 crack density functionals ($w(d) = d$ and $w(d) = d^2$, respectively).

In the experiments we will consider two variants of the TNNMG method with two different nonlinear smoothers, both based on the splitting (16) which alternates displacement and damage degrees of freedom. For the first variant—denoted

TNNMG-EX in the following—the smoother will solve the local displacement problems (20) exactly in the sense that a local (generalized) Newton iteration is used to solve the problems up to a high accuracy. In the second variant—denoted TNNMG-PRE—the smoother will solve the local displacement problems inexactly. To this end it employs a single Newton-like step with the smooth part of the functional replaced by the quadratic upper bound $(1+k)\psi_0''$. The constrained quadratic local damage problems are solved exactly by both smoothers. By Lemmas 11 and 12, both smoothers satisfy the assumptions of the convergence Theorem 4.1.

For the linear correction step (18) we use one standard $V(3,3)$ linear geometric multigrid step with a block Gauß–Seidel smoother operating on the canonical $(d+1) \times (d+1)$ blocks. Damage degrees of freedom are truncated when they are less than 10^{-10} away from their lower bound.

We measure iteration numbers, wall-time, and memory consumption. The results are compared to an operator-splitting iteration based on the \mathcal{H} -field formulation of [23], with the viscous regularization described there set to zero. That method is implemented in Fortran using the finite element program FEAP,² Version 8.3 [33]. The TNNMG algorithm is implemented in C++ using the DUNE³ libraries [4, 29].

5.1. Reformulation with a history field. The operator splitting method of [23] does not handle the pointwise non-healing constraint $\dot{d} \geq 0$ directly, but rather reformulates the problem to an unconstrained one involving the nonsmooth local history field \mathcal{H} of maximum positive reference energy. For the convenience of the reader we briefly revisit this reformulation.

It is shown in [23] that the Euler equations of the evolution (1) are

$$(22) \quad \begin{aligned} \operatorname{Div}[g(d) \boldsymbol{\sigma}_0^+(\boldsymbol{\varepsilon}) + \boldsymbol{\sigma}_0^-(\boldsymbol{\varepsilon})] &= \mathbf{0} \\ g_c \delta_d \gamma(d, \nabla d) + g'(d) \psi_0^+(\boldsymbol{\varepsilon}) + \partial_d I_{[0, \infty)}(\dot{d}) &\ni 0, \end{aligned}$$

where $\boldsymbol{\sigma}_0^\pm := \partial_\varepsilon \psi_0^\pm$ are the stresses corresponding to the split undegraded energy density, and

$$\delta_d \gamma(d, \nabla d) = c_\gamma w'(d) - \frac{w(1)}{c_l} l^2 \Delta d$$

is the variational derivative of the crack density function. The Karush–Kuhn–Tucker conditions for the variational inclusion (22) are

$$(23a) \quad \begin{aligned} \dot{d} &\geq 0 \\ -g_c \delta_d \gamma(d, \nabla d) - g'(d) \psi_0^+(\boldsymbol{\varepsilon}) &\leq 0 \end{aligned}$$

$$(23b) \quad [g_c \delta_d \gamma(d, \nabla d) + g'(d) \psi_0^+(\boldsymbol{\varepsilon})] \dot{d} = 0.$$

Assuming the derivative g' of the degradation function to be strictly negative for all $0 \leq d \leq 1$ (a property that does hold for all examples given in Section 2.1 except at the interval boundaries), we can solve (23a) for $\psi_0^+(\boldsymbol{\varepsilon})$ and get

$$(24) \quad -(g'(d))^{-1} g_c \delta_d \gamma(d, \nabla d) \geq \psi_0^+(\boldsymbol{\varepsilon}).$$

Likewise, if $\dot{d} > 0$, Equation (23b) even implies

$$-(g'(d))^{-1} g_c \delta_d \gamma(d, \nabla d) = \psi_0^+(\boldsymbol{\varepsilon}).$$

²projects.ce.berkeley.edu/feap

³www.dune-project.org

In other words, when the expression on the left of (24) changes, then its value must be equal to $\psi_0^+(\boldsymbol{\varepsilon})$. When it does not change, then $\psi_0^+(\boldsymbol{\varepsilon})$ can change independently, but by (24) it can only drop. Therefore, the left of (24) must always be equal to the maximum of $\psi_0^+(\boldsymbol{\varepsilon})$ over time. We introduce this maximum as a new quantity

$$\mathcal{H}(x, t) := \max_{s \in [0, t]} [\psi_0^+(\boldsymbol{\varepsilon}(x, s))],$$

and obtain

$$-(g'(d(x, t)))^{-1} g_c \delta_d \gamma(d(x, t), \nabla d(x, t)) = \mathcal{H}(x, t) \quad \text{for all } x \in \Omega.$$

The quantity \mathcal{H} is called the local history field of maximum positive reference energy.

With this local history field, the variational inclusion (22) for the rate independent problem can be turned into the equation

$$(25) \quad g_c \delta_d \gamma(d, \nabla d) + g'(d) \mathcal{H} = 0,$$

where the pointwise inequality constraint $\dot{d} \geq 0$ has been replaced by the history function \mathcal{H} . This history function implicitly depends on the strains and deformation at all previous times, including the current time. This dependence is nondifferentiable because of the maximum function, and therefore (25) is not inherently easier than (22).

There are various ways to approach this problem algorithmically. Miehe et al. [23] proposed to discretize (25) in a semi-implicit way, always using the value of \mathcal{H} of the previous time step. The resulting spatial problem for displacement and damage $(\mathbf{u}^{n+1}, d^{n+1})$ at the new time step t^{n+1} is then

$$(26a) \quad \text{Div}[g(d^{n+1}) \boldsymbol{\sigma}_0^+(\boldsymbol{\varepsilon}^{n+1}) + \boldsymbol{\sigma}_0^-(\boldsymbol{\varepsilon}^{n+1})] = \mathbf{0}$$

$$(26b) \quad g_c \delta_d \gamma(d^{n+1}, \nabla d^{n+1}) + g'(d^{n+1}) \mathcal{H}(\cdot, t^n) = 0,$$

which involves only differentiable functions of \mathbf{u}^{n+1} and d^{n+1} , and which can be solved without iteration. However, Miehe et al. point out that the semi-implicit character of the time discretization may slightly underestimate the speed of the crack evolution. To control this, they employ an adaptive time stepping rule, with very small loads steps near critical events.

Alternatively, one can always evaluate the \mathcal{H} -field in (26b) at the current time step t^{n+1} . In that case, the time discretization is fully implicit, but solving the nonsmooth equations (26) now requires (for example) iterating the displacement problem, the damage problem, and the update of the \mathcal{H} -field. This is the “gold standard” method termed “operator splitting” in this section on numerical experiments.

The price of the \mathcal{H} -field technique is the loss of variational structure. Unlike spatial problems of the variational time discretization of Section 3.1, the equations (26) are not the stationarity conditions of a minimization problem anymore. This makes construction and analysis of solvers more difficult.

5.2. Pure tension test of a notched, symmetric specimen. The first numerical example is a two-dimensional, square-shaped notched specimen of size $L \times L$ under tension. Due to symmetry we simulate only its upper half. Geometry and boundary conditions are shown in Figure 1. On the top edge a time-dependent normal displacement $\bar{\mathbf{u}}$ is prescribed, while the horizontal displacement is left free. The bottom edge of the lower half is clamped vertically for all $x > L/2$, and fixed

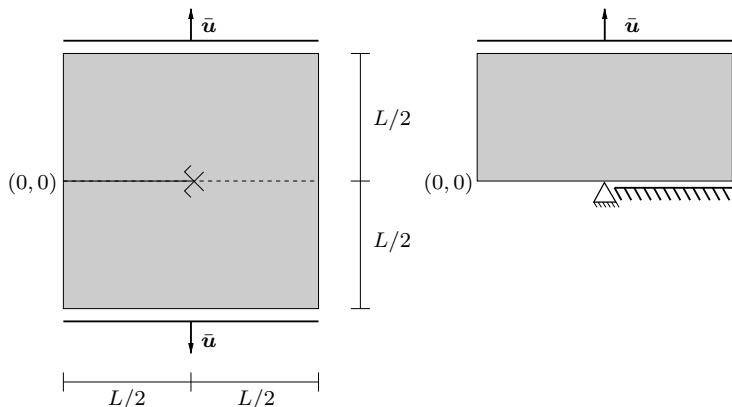


FIGURE 1. Notched square with a vertical displacement load (left). Exploiting symmetry we only simulate on the upper half of the domain (right).

vertically and horizontally at the single point $(L/2, 0)$, which is where the initial crack tip is. With increasing normal displacement \bar{u} , the preexisting crack opens, and the specimen ruptures eventually.

The simulations are performed with parameters taken from the corresponding experiment in [24], viz. $L = 1$ mm, Lamé parameters $\lambda = 121$ kN/mm² and $\mu = 80$ kN/mm², critical energy release rate $g_c = 2.7 \cdot 10^{-3}$ kN/mm, and residual stiffness $k = 10^{-5}$. The phase field regularization parameter is set to $l = 0.03125$ mm. We apply the loading in 160 steps, and set the displacement load \bar{u} at step i to

$$\bar{u}_i = i \cdot 2 \cdot 10^{-5} \text{ mm}, \quad i = 1, \dots, 160.$$

We start the evolution with no displacement and no damage anywhere.

For the spatial discretization we use three different uniform grids with 256×128 (h_1), 512×256 (h_2), and 1024×512 (h_3) quadrilateral elements, respectively. These were all constructed by uniform refinement of a grid with 32×16 elements, and hence the grid hierarchy for the multigrid solver consists of 4, 5, and 6 levels, respectively.

5.2.1. Isotropic splitting. We first consider the model with the isotropic splitting (6) of the elastic energy density, where all elastic displacements contribute to the degradation of the material. Figure 2 shows the evolution and displacement–force curves, both for the AT-1 and AT-2 functionals. The force plotted here is the total normal force on the top edge of the specimen. One can clearly see that the different formulations employed by TNNMG and operator splitting can have an impact on the evolution: Even with this relatively fine-grained loading history, the material ruptures earlier for the AT-1 model when using the \mathcal{H} -field formulation and operator-splitting instead of the variational formulation and TNNMG.

We first compare iteration numbers. At each loading step, the increment problem is solved starting from the solution of the previous time step until the energy norm of the correction normalized by the energy norm of the previous iterate drops below 10^{-7} . The upper row of Figure 3 shows the number of iterations for the TNNMG solver with the exact smoother (TNNMG-EX), with logarithmically scaled vertical

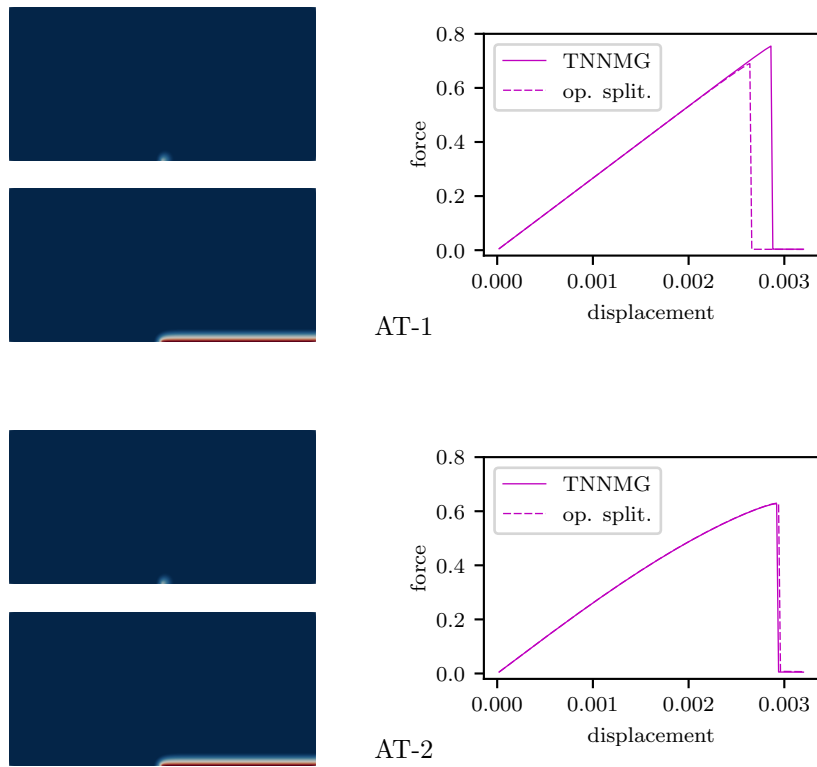


FIGURE 2. 2d example, isotropic energy split: Evolution at time steps 145 and 160 computed with the TNNMG algorithm, and displacement–force curves for the AT-1 (top) and AT-2 (bottom) models

axis. As can be seen, the iteration numbers remain essentially bounded independently from the grid resolution. The peak shortly before the 150th load step is where the material ruptures. In this situation, the system becomes highly unstable, which translates to a higher number of iterations.

After the rupture, the iteration numbers do depend on the mesh resolution. This is atypical for a multigrid solver—presumably it is caused by the fact that, given the particular boundary conditions, the completely ruptured specimen is essentially an ill-posed problem. Curiously, though, observe that this effect cannot be seen when using the spectrally-split energy density (Figure 6).

For comparison, the lower row of Figure 3 shows the iteration numbers of the operator splitting method. One can see that for the first two thirds of the loading history, this method needs less iterations than the TNNMG algorithm, and that iteration numbers are independent from the grid resolution. Recall, however, that TNNMG iterations are much cheaper than operator-splitting iterations, because they are essentially single multigrid iterations, whereas each operator-splitting iteration involves solving two global linear systems. In contrast to the TNNMG method, the number of iterations increases with increasing load, and shortly before

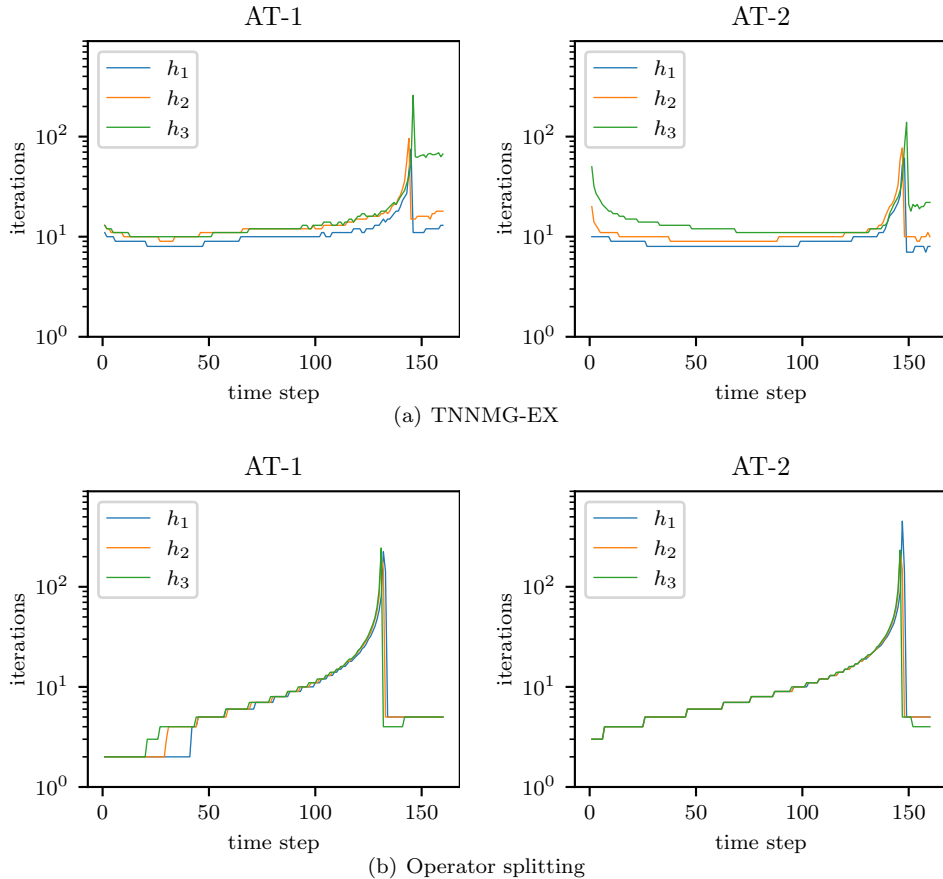


FIGURE 3. 2d example, isotropic energy split: Iterations per time step

the peak iteration numbers are higher. At the peak itself, iteration numbers exceed the number of the TNNMG method.

We do not show the iteration numbers of TNNMG with the inexact smoother, because they virtually coincide with the results for TNNMG-EX. This is not surprising: As the model uses the isotropic split of the elastic energy, the local displacement problems are quadratic, and a single Newton step suffices. TNNMG-PRE simply uses a preconditioner for those quadratic problems, which does not have a significant impact on the smoothing and thus on the speed of convergence. However, since the preconditioner is independent of the current iterate, the corresponding local matrices can be precomputed.

Wall-time behavior is discussed next. We plot wall-time per time step for the two multigrid variants TNNMG-EX and TNNMG-PRE, and for the operator-splitting method (Figure 4, again with logarithmic vertical axis). The plots show the time normalized by the number of degrees of freedom, to highlight the complexity difference between the two solvers.⁴ We see that TNNMG beats operator-splitting by more than an order of magnitude. What is more, the time per degree of freedom

⁴Note that we are also comparing two different implementations here!

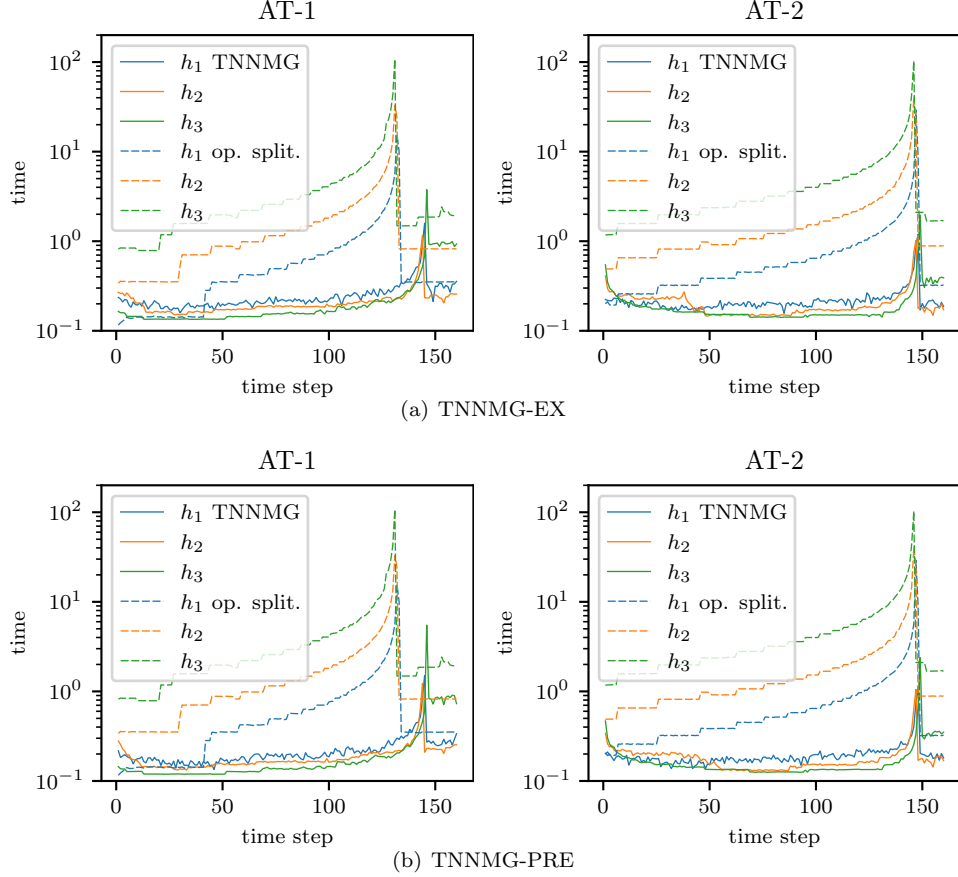


FIGURE 4. 2d example, isotropic energy split: Wall-time per degree of freedom per time step

	AT-1			AT-2		
	TNNMG-EX	TNNMG-PRE	OS	TNNMG-EX	TNNMG-PRE	OS
h_1	40.19	35.37	119.93	35.23	31.40	144.62
h_2	33.67	30.33	283.31	32.26	29.08	323.32
h_3	42.20	39.42	658.53	31.97	29.02	765.91

TABLE 1. 2d example, isotropic energy split: Total wall time per degree of freedom

stays roughly constant for the multigrid method, independent of the grid resolution, whereas it increases by a factor of approximately 2.3 for the operator splitting, for each additional step of refinement. This is caused by the well-known superlinear time complexity of the direct sparse solver used by FEAP. Table 1 shows the accumulated normal run-times for the entire load history. It shows that the speed differences for the h_3 grid accumulate to a factor of about 16 (AT-1) and 25 (AT-2).

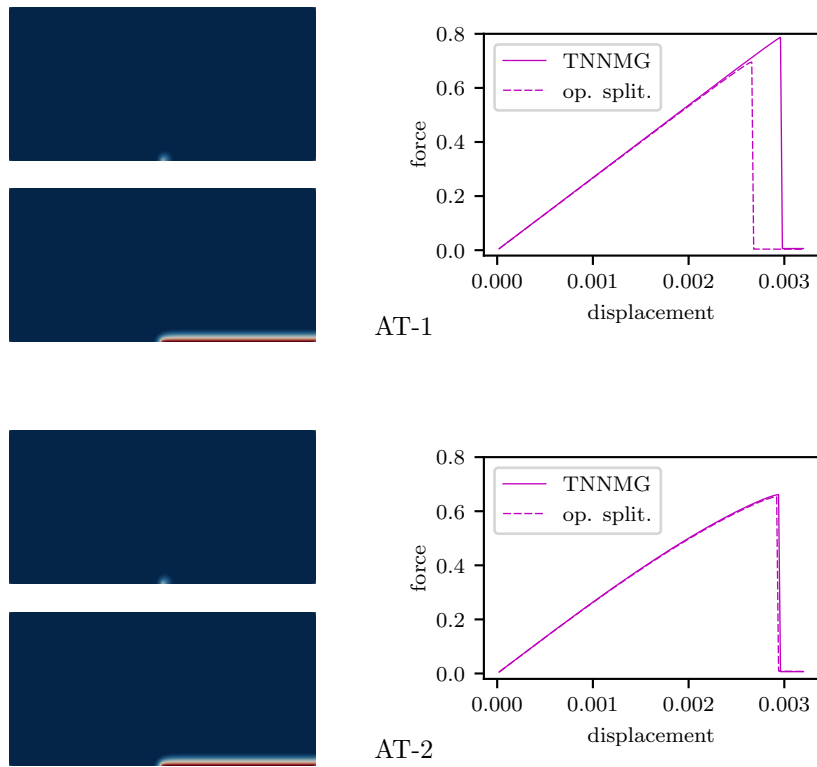


FIGURE 5. 2d example, spectral energy split: Evolution at time steps 145 and 160, and displacement–force curves for the AT-1 (top) and AT-2 (bottom) models

Figure 4 and Table 1 also show the wall-times for TNNMG-PRE, the TNNMG variant using an inexact local solver. It can be observed that using that smoother does lead to lower computation times, but the effect is minor. As the computational efforts largely coincide—up to the precomputation of local preconditioned Hessians in TNNMG-PRE—this is not surprising.

Finally, we point out that the AT-1 functional is solved with the same efficiency as the AT-2 one, even though the threshold for damage formation makes it more challenging.

5.2.2. Spectral splitting of the elastic energy density. For the next experiment we exchange the isotropic energy split (6) by the spectral one (9). As the example specimen is loaded in tension we expect few differences to the previous experiments, and indeed, the displacement–load curves (in Figure 5) show only minor differences compared to the ones of the isotropic splitting (Figure 2).

The purpose of this test is primarily to assess the cost of the two-dimensional eigenvalue decomposition and its derivatives required for the spectral split. Figure 6 shows the iteration numbers per time step for the three methods. As the model is not quadratic in the displacement anymore, we now distinguish between the TNNMG-EX and the TNNMG-PRE smoothers. Not surprisingly though, the

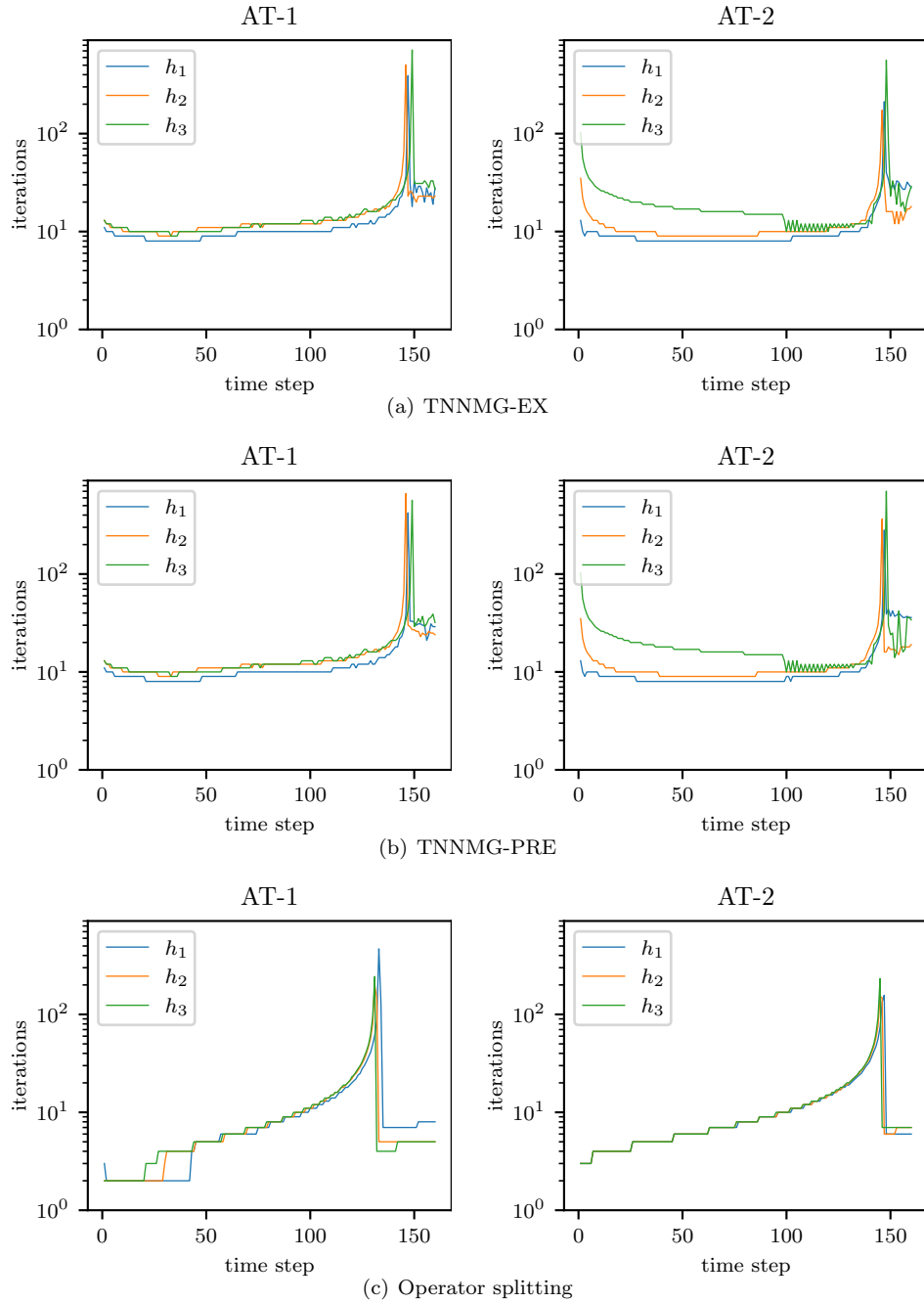


FIGURE 6. 2d example, spectral energy split: Iterations per time step

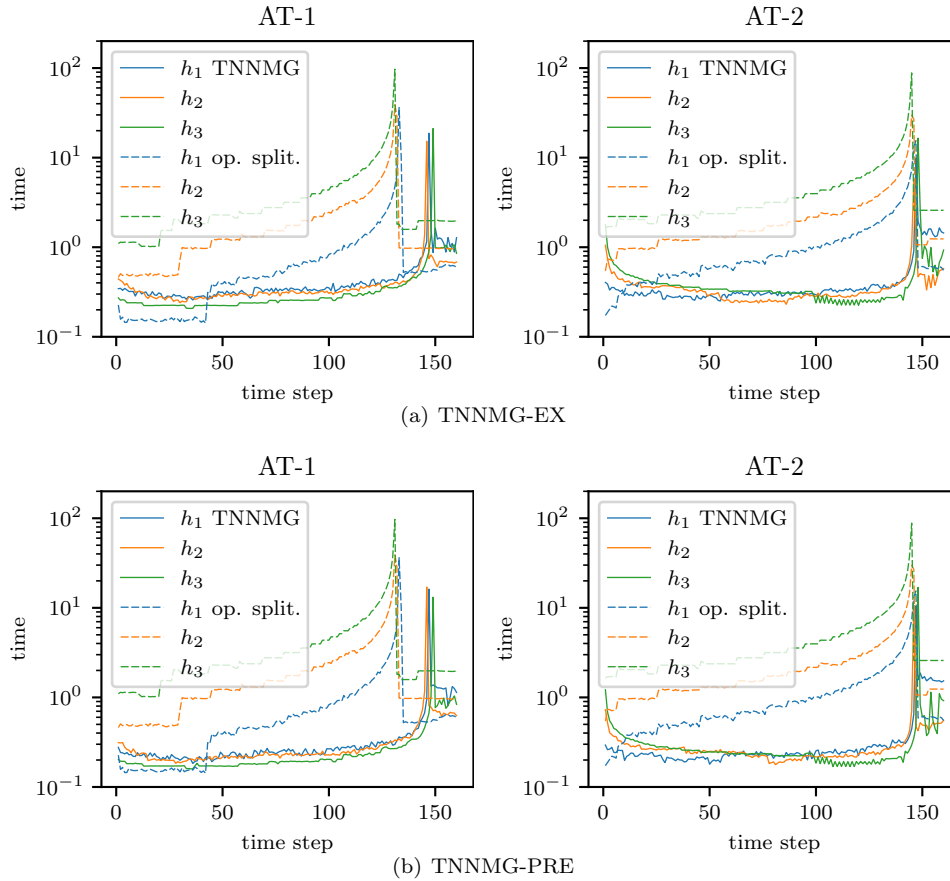


FIGURE 7. 2d example, spectral energy split: Wall-time per degree of freedom per time step

iteration numbers are virtually identical. The iterations needed by the operator splitting method, shown in the lowest row of Figure 6, have not changed appreciably either.

We turn to wall-time: Figure 7 shows the time needed to solve the increment problems, again normalized by the number of degrees of freedom. One can see that the overall behavior remains unchanged. The time needed by TNNMG goes up a little bit, but the method remains vastly faster than operator splitting. Interestingly, the operator splitting solver for the AT-2 problem is a bit faster during the rupturing of the specimen than it was for the isotropically split energy.

Table 2 shows the total run-time of the simulations, still normalized by the number of degrees of freedom. We can still observe the complexity difference between the TNNMG and operator splitting solvers. Here, the inexact smoother used by TNNMG-PRE really does help to save run-time, because it avoids the costly eigenvalue decomposition. The speedup is appreciable, even though in two space dimensions an eigenvalue decomposition is not all that expensive.

	AT-1			AT-2		
	TNNMG-EX	TNNMG-PRE	OS	TNNMG-EX	TNNMG-PRE	OS
h_1	86.85	70.92	155.32	76.82	66.75	186.58
h_2	73.61	63.83	353.63	61.63	54.91	387.06
h_3	74.55	54.98	672.26	80.25	63.27	760.48

TABLE 2. 2d example, spectral energy split: Total wall time per degree of freedom

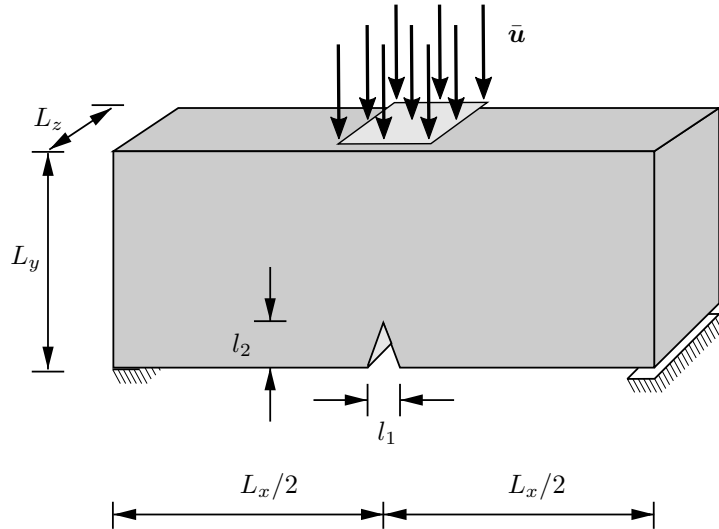


FIGURE 8. Boundary value problem of bending test in three dimensions

5.3. Bending test of a notched bar in three dimensions. The second example uses a three-dimensional object. In three dimensions, stiffness matrices get denser, and hence direct solvers for global linear systems get more expensive and need considerably more memory. In contrast, the TNNMG memory consumption remains linear in the number of unknowns. Also, eigenvalue decompositions are more expensive for 3×3 matrices, and we therefore expect larger run-time differences between the isotropic and the spectrally split model, and between the two TNNMG smoothers.

We consider a bending test for a rectangular bar with a triangular notch. In this setting, the decomposition of the elastic energy density plays a crucial role. Under the given loading, parts of the specimen undergo severe compression, and material models that degrade under such compression will therefore show unphysical results. We test the solvers with the isotropic splitting (6) nevertheless, to obtain an idea of the cost of the spectral splitting.

The example setting is again taken from [24]. The geometry and the boundary conditions are visualized in Figure 8. The dimensions of the specimen are $L_x = 8$ mm, $L_y = 2$ mm and $L_z = 1$ mm. Width and height of the triangular notch are $l_1 = 0.4$ mm and $l_2 = 0.2$ mm, respectively. We use two different unstructured hexahedral grids to discretize the domain, one with 20 480 and one with 122 880

elements. In the figures these are denoted by h_1 and h_2 , respectively. The grids were constructed by 3 and 4 steps of uniform refinement of two different coarse grids with 40 and 30 hexahedral elements, respectively, and this refinement history is used by the linear geometric multigrid step of the TNNMG algorithm. We do not test further refinement of these grids, because the corresponding operator-splitting simulations would not fit into the 32 GB of main memory available on our testing machine.

As in [24], the Lamé parameters are set to $\lambda = 121 \text{ kN/mm}^2$ and $\mu = 80 \text{ kN/mm}^2$. For the further parameters we set $g_c = 2.7 \cdot 10^{-3} \text{ kN/mm}$, $l = 0.2 \text{ mm}$, and $k = 10^{-5}$. The object is loaded with a time-dependent displacement load in downward direction in a strip of width 1.2 mm in the center of the top surface. In that strip, the surface is fixed in z -direction, but free to move in x -direction. The displacement load is set to $\bar{\mathbf{u}}_i = -5 \cdot 10^{-3} \text{ mm} \cdot i$ for the load steps $i = 1, \dots, 13$. No adaptive load-stepping as in [24] is necessary, because time discretization and solvers are stable enough for this range of load step sizes. The object is fully clamped at a strip of width 0.4 mm at the left end of the lower surface. At the right end of the same surface, a strip of width 0.4 mm is fixed in the y and z directions.

For each time step, we solve the increment problem with the same solver settings as for the two-dimensional example: Each iteration starts at the solution of the previous load step, and we terminate when the energy norm of the correction, scaled by the energy norm of the previous iterate, drops below 10^{-7} . The linear correction step (18) is a geometric multigrid $V(3,3)$ -cycle step with a block-Gauß-Seidel smoother, and damage degrees of freedom are truncated when their current value is less than 10^{-10} away from the lower obstacle.

5.3.1. Isotropic splitting. We first consider the model with the isotropic splitting (6) of the elastic energy density, i.e., the model where all elastic displacements contribute to the degradation of the material. We expect unphysical results: Virtually all damage will happen in the vicinity of the load, whereas the region around the notch will remain intact. We are nevertheless interested in the solver behavior for this model, primarily to assess the cost of the spectral splitting in the next section. No costly eigenvalue decompositions are necessary for the isotropic splitting considered here, and the local displacement problems (21) are quadratic. Consequently, the two smoother variants TNNMG-EX and TNNMG-PRE solve almost the same problems, and we expect them to behave more or less the same, too, with a small run-time advantage for TNNMG-PRE.

Figure 9 shows the reaction force as a function of the applied displacement, both for the AT-1 and AT-2 models. Unlike the other displacement–force plots in this text, Figure 9 shows three curves per model. Two of them are for the TNNMG and operator-splitting methods as previously. Curiously, they exhibit completely different force evolutions. While the operator-splitting curve shows a prominent peak, the TNNMG curve exhibits a monotonic decrease of the reaction force. This shows that the biconvex increment functional (13) can really have more than one local minimizer, and that convergent solution algorithms will pick one of them in a way that is difficult to control in practice.

In this particular case the first step of the TNNMG method is the local smoother, which modifies displacement and damage variables vertex by vertex. When first handling the vertices with prescribed displacement, the large local residual there leads to immediate damage formation. In contrast, the operator-splitting method

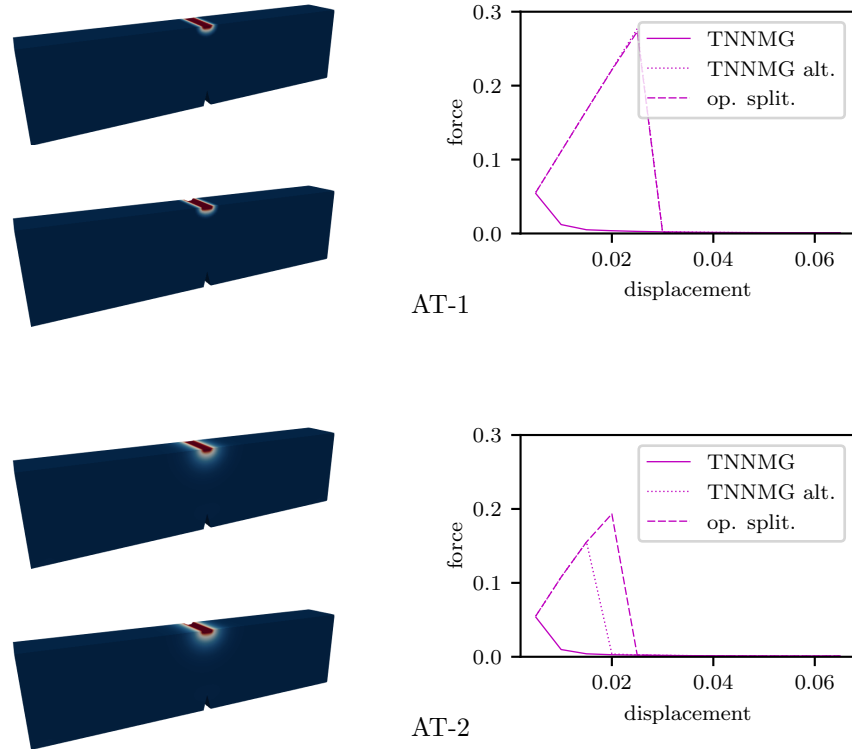


FIGURE 9. 3d example, isotropic energy split: Configurations at load steps 1 and 11, and displacement–force curves. The damage distributions on the left were computed using TNNMG without modification of the initial iterates, and correspond to the displacement–force curves without peak.

starts by solving a global displacement problem. This distributes the stresses caused by the prescribed displacement more evenly across the object, and the subsequent damage step does not lead to relevant damage formation until several load steps later.

To corroborate this hypothesis, we perform a second simulation with the TNNMG solver, where, rather than directly starting from the solution of the previous load step, we first apply one linear multigrid iteration to the displacement problem before starting the TNNMG solver. The result is marked as “TNNMG alt.” in Figure 9. It can be seen that the initial displacement multigrid step is enough to sufficiently distribute the stressed caused by the boundary condition, and the force now shows the same behavior as when using the operator-splitting iteration.

Nevertheless, for the sake of consistency, all subsequent simulations start again from the solution of the previous load step. To assess solver performance, we again first compare iteration numbers. Figure 10 shows the iteration numbers per time step needed by the two TNNMG variants, and by the operator-splitting iteration. Note again that the vertical axis is scaled logarithmically. One can see that all

	AT-1			AT-2		
	TNNMG-EX	TNNMG-PRE	OS	TNNMG-EX	TNNMG-PRE	OS
h_1	14.89	12.95	96.08	12.45	14.73	107.14
h_2	24.46	22.98	975.18	19.62	15.27	1149.63

TABLE 3. 3d example, isotropic energy split: Total wall time per degree of freedom

methods need roughly the same number of iterations, and the required number of iterations is similar for all load steps.

When comparing wall-times, however, the situation changes. The time difference between a single multigrid iteration and solving two global linear systems of equations is even more dramatic now that the underlying PDE is defined on a three-dimensional domain. As a consequence, even on the coarse example grid the operator splitting takes ten times as much time for solving the increment problem as the TNNMG algorithm. What is more, for the finer grid this ratio increases to a factor of 100. This increase is due to the superlinear complexity of the sparse linear solver employed by the operator splitting algorithm. In contrast, the wall-time per degree of freedom remains roughly constant for the multigrid method, which is a typical behavior.

5.3.2. Spectral splitting of the elastic energy density. In the second set of experiments we replace the unsplit degraded energy density (6) by the one with the spectral split according to (9). Figure 12 shows two snapshots from the problem evolution, and the reaction force as a function of the applied displacement. One can clearly see the differences to the simulation with the unsplit energy. As one would expect, the damage now happens primarily near the notch, and the peak in the displacement–force curve is more prominent.

Figure 13 shows the iteration numbers for TNNMG with both smoothers and the operator-splitting method again. Iteration numbers for all three algorithms and both AT models are roughly the same. In particular, TNNMG-PRE, the multigrid method with the inexact smoother avoiding the costly 3×3 eigenvalue decomposition, does not need more iterations than TNNMG-EX.

When looking at wall-times, the TNNMG-PRE algorithm can finally show its full potential. Figure 7 shows the normalized times in the same way as in the previous sections. Again, the time per degree of freedom is roughly constant for the multigrid algorithms, whereas it grows with increasing grid resolution for operator splitting. This translates to a speedup of about 50 for TNNMG-EX compared to operator splitting. This speedup can be seen both for AT-2 and the more challenging AT-1 model. The TNNMG-PRE algorithm is even faster, however. It requires the same number of iterations, but each iteration is much cheaper. From Table 4 with the accumulated total normalized times one can see that TNNMG-PRE can solve both the AT-1 and the AT-2 problems in less than 1% of the time required by operator splitting.

Finally, we investigate the memory consumption of the two solver implementations. Figure 15 shows the maximum amount of memory used by the two algorithms for the two test grids, tested with the `gnome-system-monitor` program. One can

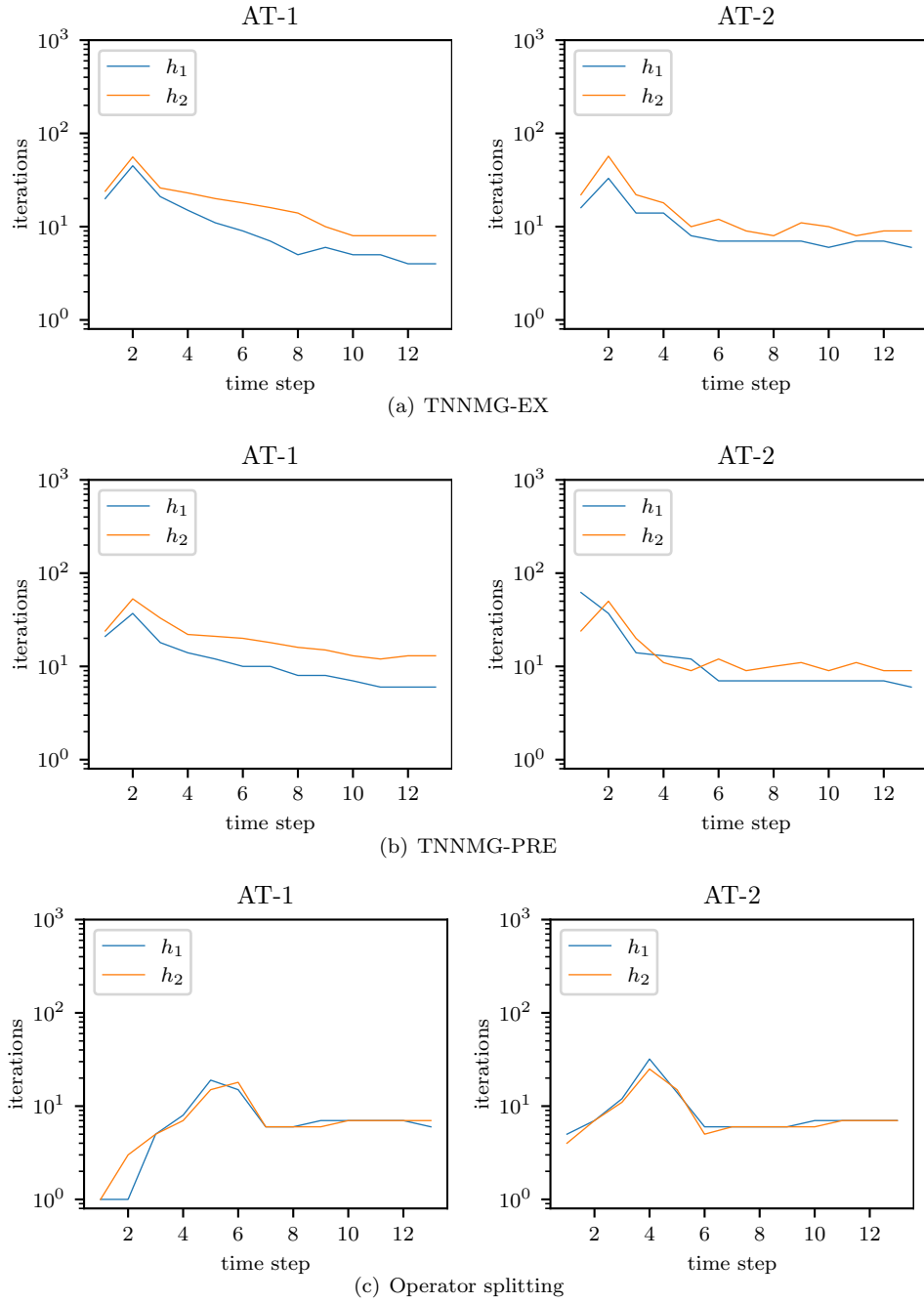


FIGURE 10. 3d example, isotropic energy split: Iterations per time step

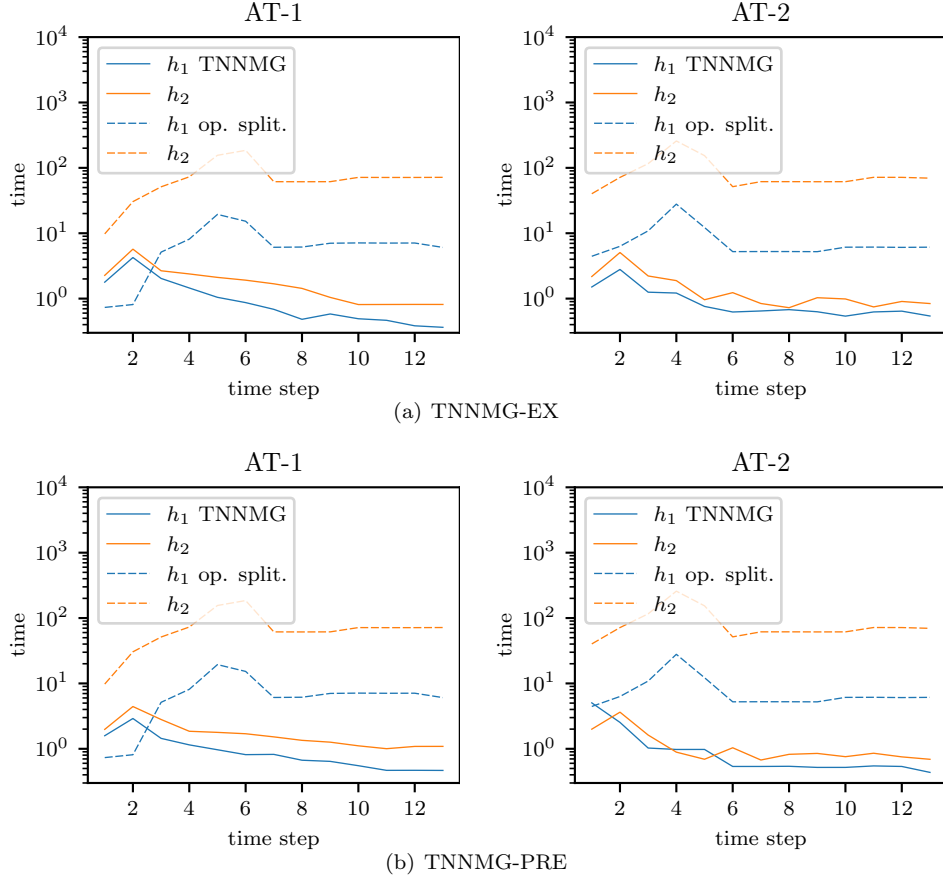


FIGURE 11. 3d example, isotropic energy split: Wall-time per degree of freedom over time step

	AT-1			AT-2		
	TNNMG-EX	TNNMG-PRE	OS	TNNMG-EX	TNNMG-PRE	OS
h_1	168.47	94.18	1158.98	231.08	112.79	1058.21
h_2	216.32	120.18	10762.81	366.24	195.85	12309.42

TABLE 4. 3d example, spectral energy split: Total wall time per degree of freedom

see that even for the moderate problem sizes considered here, operator splitting requires twice as much memory as the multigrid algorithm.

Comparing with similar measurements as in, e.g., [30], the difference is smaller than expected. This is because the smooth part \mathcal{J}_0 of the functional considered in [30] is quadratic, which is in contrast to the more general functional considered here. In order to obtain first- and second-order derivatives efficiently during the local solves, our implementation precomputes and stores the values and derivatives of the shape functions at all quadrature points (what Miehe et al. call the *global*

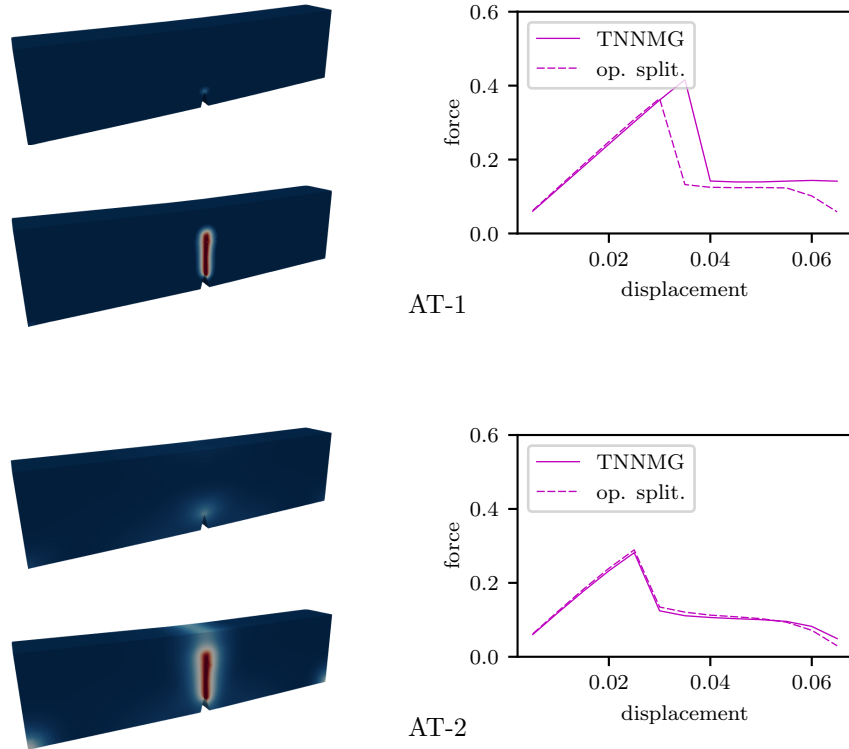


FIGURE 12. 3d example, spectral energy split: Evolution at time steps 1 and 11, and displacement–force curves

interpolation matrix [23, Chap. 4.2]). This requires a considerable amount of memory. We point out, however, that the memory consumption remains linear in the problem size. More efficient implementations are subject of ongoing work.

REFERENCES

- [1] M. Ambati, T. Gerasimov, and L. D. Lorenzis. A review on phase-field models of brittle fracture and a new fast hybrid formulation. *Comput Mech*, 55:383–405, 2015. doi: 10.1007/s00466-014-1109-y.
- [2] H. Amor, J.-J. Marigo, and C. Maurini. Regularized formulation of the variational brittle fracture with unilateral contact: Numerical experiments. *J Mech Phys Solids*, 57(8):1209–1229, 2009. doi: 10.1016/j.jmps.2009.04.011.
- [3] M. Baes. Convexity and differentiability properties of spectral functions and spectral mappings on Euclidean Jordan algebras. *Linear Algebra and its Applications*, 422(2):664–700, 2007. doi: 10.1016/j.laa.2006.11.025.
- [4] P. Bastian, M. Blatt, A. Dedner, N.-A. Dreier, C. Engwer, R. Fritze, C. Gräser, C. Grüniger, D. Kempf, R. Klöfkorn, M. Ohlberger, and O. Sander. The DUNE framework: Basic concepts and recent developments. *Computers &*

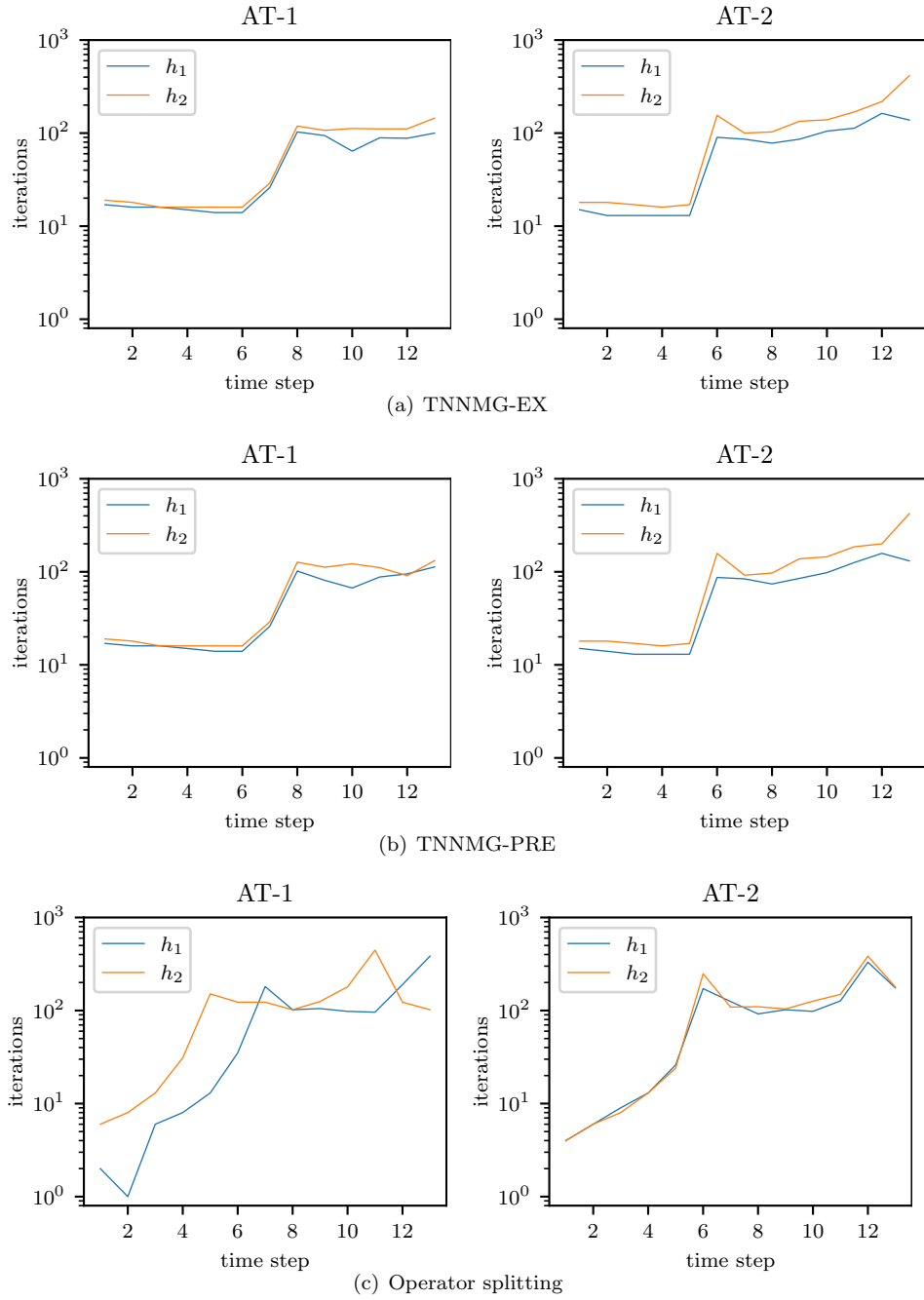


FIGURE 13. 3d example, spectral energy split: Iterations per time step

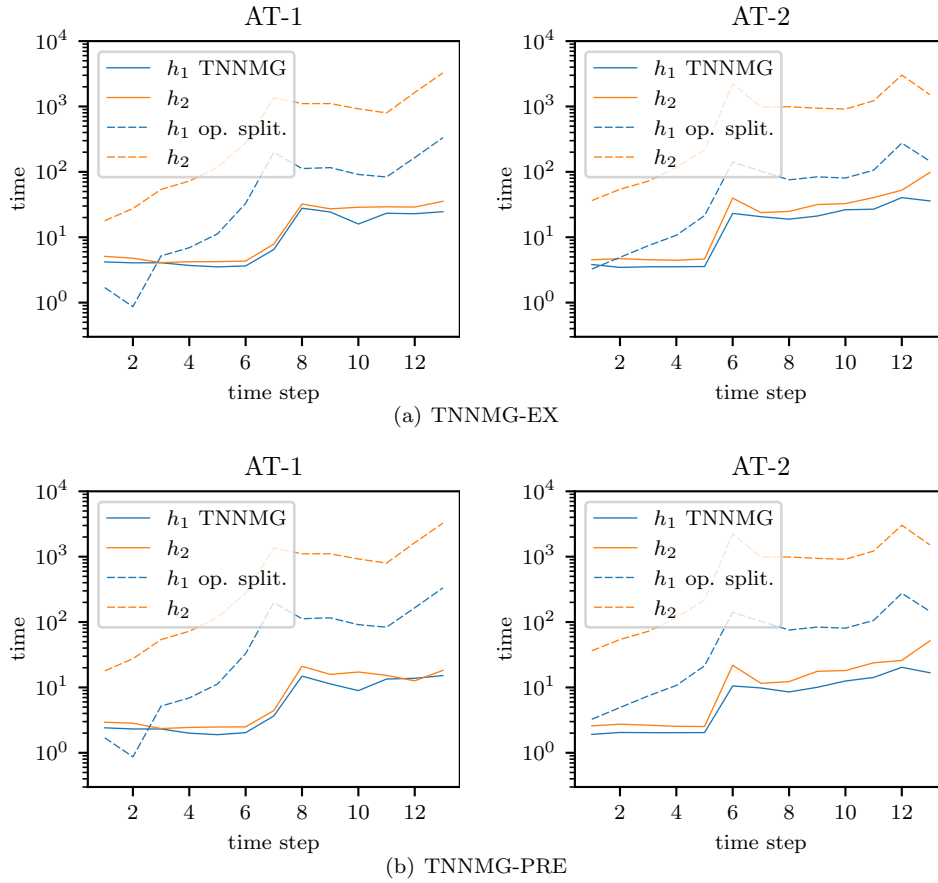


FIGURE 14. 3d example, spectral energy split: Wall-time per degree of freedom over time step

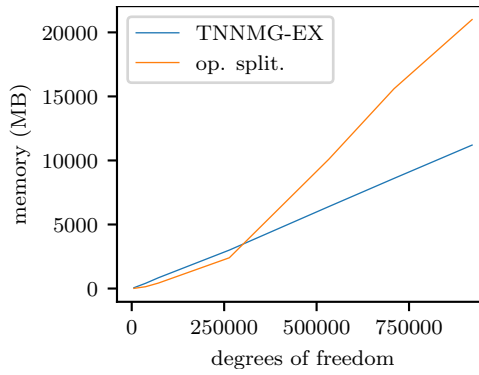


FIGURE 15. 3d example, spectral energy split: Memory consumption for solving one increment problem of the AT-2 functional

- Mathematics with Applications*, 81:75–112, 2021. doi: 10.1016/j.camwa.2020.06.007.
- [5] B. Bourdin. Numerical implementation of the variational formulation for quasi-static brittle fracture. *Interfaces and free boundaries*, 9(3):411–430, 2007.
 - [6] B. Bourdin, G. Francfort, and J. J. Marigo. Numerical experiments in revisited brittle fracture. *J Mech Phys Solids*, 48:797–826, 2000.
 - [7] S. Burke, C. Ortner, and E. Süli. An adaptive finite element approximation of a variational model of brittle fracture. *SIAM Journal on Numerical Analysis*, 48(3):980–1012, 2010.
 - [8] B. Dacorogna. *Direct methods in the calculus of variations*. Springer, first edition, 1989.
 - [9] P. Farrell and C. Maurini. Linear and nonlinear solvers for variational phase-field models of brittle fracture. *Int. J. Numer. Meth. Engng*, 109(5):648–667, 2017.
 - [10] T. Gerasimov and L. De Lorenzis. A line search assisted monolithic approach for phase-field computing of brittle fracture. *Comput. Methods Appl. Mech. Engrg.*, 312:276–303, 2016.
 - [11] T. Gerasimov and L. De Lorenzis. On penalization in variational phase-field models of brittle fracture. *Comput. Methods Appl. Mech. Engrg.*, 354:990–1026, 2019. doi: 10.1016/j.cma.2019.05.038.
 - [12] R. Glowinski. *Numerical Methods for Nonlinear Variational Problems*. Springer Series in Computational Physics. Springer, third edition, 1984.
 - [13] C. Gräser and R. Kornhuber. Multigrid methods for obstacle problems. *J. Comp. Math.*, 27(1):1–44, 2009.
 - [14] C. Gräser and O. Sander. Truncated nonsmooth Newton multigrid methods for simplex-constrained minimization problems. Preprint 384, IGPM Aachen, 2014.
 - [15] C. Gräser and O. Sander. Truncated nonsmooth Newton multigrid methods for block-separable minimization problems. *IMA J. Numer. Anal.*, 39:454–481, 2019. doi: 10.1093/imanum/dry073.
 - [16] C. Gräser, U. Sack, and O. Sander. Truncated nonsmooth Newton multigrid methods for convex minimization problems. In M. Bercovier, M. Gander, R. Kornhuber, and O. Widlund, editors, *Domain Decomposition Methods in Science and Engineering XVIII*, volume 70 of *Lecture Notes in Computational Science and Engineering*. Springer, 2009.
 - [17] T. Heister, M. F. Wheeler, and T. Wick. A primal–dual active set method and predictor–corrector mesh adaptivity for computing fracture propagation using a phase-field approach. *Comput. Methods Appl. Mech. Engrg.*, 290:466–495, 2015. doi: 10.1016/j.cma.2015.03.009.
 - [18] A. Kopaničáková and R. Krause. A recursive multilevel trust region method with application to fully monolithic phase-field models of brittle fracture. *Comput. Methods Appl. Mech. Engrg.*, 360:112720, 2020. doi: <https://doi.org/10.1016/j.cma.2019.112720>.
 - [19] R. Kornhuber. *Adaptive monotone multigrid methods for nonlinear variational problems*. Vieweg + Teubner Verlag, 1997. ISBN 3519027224.
 - [20] C. Kuhn, A. Schlüter, and R. Müller. On degradation functions in phase field fracture models. *Computational Materials Science*, 108:374–384, 2015.

- [21] G. Lancioni and G. Royer-Carfagni. The variational approach to fracture mechanics. A practical application to the french Panthéon in Paris. *J Elast*, 95:1–30, 2009. doi: 10.1007/s10659-009-9189-1.
- [22] S. May, J. Vignollet, and R. de Borst. A new arc-length control method based on the rates of the internal and the dissipated energy. *Engineering Computations*, 33(1):100–115, 2016.
- [23] C. Miehe, M. Hofacker, and F. Welschinger. A phase field model for rate-independent crack propagation: Robust algorithmic implementation based on operator splits. *Comput. Methods Appl. Mech. Engrg.*, 199:2765–2778, 2010.
- [24] C. Miehe, F. Welschinger, and M. Hofacker. Thermodynamically consistent phase-field models of fracture: Variational principles and multi-field FE implementations. *Int. J. Numer. Meth. Engrg*, 83:1273–1311, 2010.
- [25] A. Mielke and T. Roubíček. *Rate-Independent Systems*. Springer, 2015.
- [26] K. Pham, H. Amor, J.-J. Marigo, and C. Maurini. Gradient damage models and their use to approximate brittle fracture. *International Journal of Damage Mechanics*, 20(4):618–652, 2011. doi: 10.1177/1056789510386852.
- [27] H. Qi and X. Yang. Semismoothness of spectral functions. *SIAM Journal on Matrix Analysis and Applications*, 25(3):766–783, 2003.
- [28] L. Qi and J. Sun. A nonsmooth version of Newton’s method. *Math. Prog.*, 58:353–367, 1993.
- [29] O. Sander. *DUNE — The Distributed and Unified Numerics Environment*, volume 140 of *LNCSE*. Springer, 2020. doi: 10.1007/978-3-030-59702-3.
- [30] O. Sander and P. Jaap. Solving primal plasticity increment problems in the time of a single predictor–corrector iteration. *Comput. Mech.*, 2019. doi: 10.1007/s00466-019-01788-y.
- [31] N. Singh, C. Verhoosel, R. de Borst, and E. van Brummelen. A fracture-controlled path-following technique for phase-field modeling of brittle fracture. *Finite Elements in Analysis and Design*, 113:14–29, 2016. doi: 10.1016/j.finel.2015.12.005.
- [32] C. Steinke and M. Kaliske. A phase-field crack model based on directional stress decomposition. *Computational Mechanics*, pages 1–28, 2018.
- [33] R. L. Taylor. *FEAP – A Finite Element Analysis Program*. Version 8.3 User Manual, University of California at Berkeley, 2011.
- [34] M. Ulbrich. *Nonsmooth Newton-like Methods for Variational Inequalities and Constrained Optimization Problems in Function Spaces*. Habilitationsschrift, Technische Universität München, 2002.
- [35] M. Wheeler, T. Wick, and W. Wollner. An augmented-Lagrangian method for the phase-field approach for pressurized fractures. *Comput. Methods Appl. Mech. Engrg.*, 271:69–85, 2014.
- [36] T. Wick. An error-oriented Newton/inexact augmented Lagrangian approach for fully monolithic phase-field fracture propagation. *SIAM Journal on Scientific Computing*, 39(4):B589–B617, 2017.
- [37] T. Wick. Modified Newton methods for solving fully monolithic phase-field quasi-static brittle fracture propagation. *Comput. Methods Appl. Mech. Engrg.*, 325:577–611, 2017. doi: 10.1016/j.cma.2017.07.026.
- [38] J. Wu. Numerical implementation of non-standard phase-field damage models. *Comput. Methods Appl. Mech. Engrg.*, 340:767–797, 2018.

- [39] J.-Y. Wu, Y. Huang, and V. P. Nguyen. On the BFGS monolithic algorithm for the unified phase field damage theory. *Comput. Methods Appl. Mech. Engrg.*, 360:112704, 2020. doi: 10.1016/j.cma.2019.112704.

CARSTEN GRÄSER, FREIE UNIVERSITÄT BERLIN, INSTITUT FÜR MATHEMATIK, ARNIMALLEE 6, 14195 BERLIN, GERMANY

Email address: `graeser@mi.fu-berlin.de`

DANIEL KIENLE, UNIVERSITÄT STUTTGART, INSTITUT FÜR ANGEWANDTE MECHANIK, PFAFFENWALDRING 7, 70569 STUTTGART, GERMANY

Email address: `kienle@mechbau.uni-stuttgart.de`

OLIVER SANDER, TECHNISCHE UNIVERSITÄT DRESDEN, INSTITUT FÜR NUMERISCHE MATHEMATIK, ZELLESCHER WEG 12–14, 01069 DRESDEN, GERMANY

Email address: `oliver.sander@tu-dresden.de`